

This article has been accepted for publication in Monthly Notices of the Royal Astronomical Society ©: 2019 The Authors. Published by Oxford University Press on behalf of the Royal Astronomical Society. All rights reserved.

The Pristine survey – IX. CFHT ESPaDOnS spectroscopic analysis of 115 bright metal-poor candidate stars

Kim A. Venn^{1,2,3}★, Collin L. Kielty¹, Federico Sestito^{2,3}, Else Starkenburg³,
 Nicolas Martin^{2,4}, David S. Aguado⁵, Anke Arentsen³, Piercarlo Bonifacio⁶,
 Elisabetta Caffau⁶, Vanessa Hill⁷, Pascale Jablonka^{6,8}, Carmela Lardo⁸,
 Lyudmilla Mashonkina⁹, Julio F. Navarro¹, Chris Sneden¹⁰, Guillaume Thomas¹¹,
 Kris Youakim³, Jonay I. González-Hernández^{12,13}, Rubén Sánchez Janssen¹⁴,
 Ray Carlberg¹⁵ and Khyati Malhan¹⁶

Affiliations are listed at the end of the paper

Accepted 2019 December 10. Received 2019 December 10; in original form 2019 October 12

ABSTRACT

A chemo-dynamical analysis of 115 metal-poor candidate stars selected from the narrow-band *Pristine* photometric survey is presented based on CFHT high-resolution ESPaDOnS spectroscopy. We have discovered 28 new bright ($V < 15$) stars with $[\text{Fe}/\text{H}] < -2.5$ and 5 with $[\text{Fe}/\text{H}] < -3.0$ for success rates of 40 (28/70) and 19 per cent (5/27), respectively. A detailed model atmosphere analysis is carried out for the 28 new metal-poor stars. Stellar parameters were determined from SDSS photometric colours, *Gaia* DR2 parallaxes, MESA/MIST stellar isochrones, and the initial *Pristine* survey metallicities, following a Bayesian inference method. Chemical abundances are determined for 10 elements (Na, Mg, Ca, Sc, Ti, Cr, Fe, Ni, Y, and Ba). Most stars show chemical abundance patterns that are similar to the normal metal-poor stars in the Galactic halo; however, we also report the discoveries of a new r-process-rich star, a new CEMP-s candidate with $[\text{Y}/\text{Ba}] > 0$, and a metal-poor star with very low $[\text{Mg}/\text{Fe}]$. The kinematics and orbits for all of the highly probable metal-poor candidates are determined by combining our precision radial velocities with *Gaia* DR2 proper motions. Some stars show unusual kinematics for their chemistries, including planar orbits, unbound orbits, and highly elliptical orbits that plunge deeply into the Galactic bulge ($R_{\text{peri}} < 0.5$ kpc); also, eight stars have orbital energies and actions consistent with the *Gaia*-Enceladus accretion event. This paper contributes to our understanding of the complex chemo-dynamics of the metal-poor Galaxy, and increases the number of known bright metal-poor stars available for detailed nucleosynthetic studies.

Key words: Galaxy: stellar content – Galaxy: kinematics and dynamics – Galaxy: abundances – stars: Population II – stars: abundances – stars: kinematics and dynamics.

1 INTRODUCTION

Very old stars are witness to the earliest epochs of galaxy formation and evolution. Most theoretical models of star formation at early times predict the formation of high-mass stars (e.g. Nakamura & Umemura 2001; Abel, Bryan & Norman 2002; Bromm 2013) that contributed to the reionization of the Universe. During their short lives, these massive stars initiate the formation of the chemical elements beyond hydrogen, helium, and lithium, and yet no star

with such a primordial composition has yet been found. The fragmentation of the early star-forming regions has also been predicted (e.g. Schneider et al. 2003; Clark et al. 2011; Greif 2015; Hirano et al. 2015), providing an environment where lower mass ($\sim 1 M_{\odot}$) stars could form, which would have much longer lifetimes. These old stars are expected to be metal poor, having formed from nearly pristine gas, and could be used to trace the chemical elements from the massive (first) stars and their subsequent supernovae (e.g. Frebel & Norris 2015; Hartwig et al. 2018; Salvadori et al. 2019).

In recent years, abundance patterns of metal-poor stars have been examined extensively (e.g. Keller et al. 2014; Ishigaki et al. 2018;

* E-mail: kvenn@uvic.ca

Nordlander et al. 2019), pointing to the significance of low-energy (faint) supernovae, whose ejecta fall back on to their iron cores, thereby mainly expelling light elements. It is not clear if these low-energy supernovae were more common at ancient times, or if concurrent massive stars underwent direct collapse to black holes and ceased nearby star formation, erasing any direct evidence of their presence in the next generation of stars. Overall, metal-poor stars allow us to examine nucleosynthetic yields from one or a few supernova events to constrain the detailed physics of these events, such as neutron star masses, rotation rates, mixing efficiencies, explosion energies, etc. (Heger & Woosley 2010; Thielemann et al. 2018; Wanajo 2018; Jones et al. 2019; Müller et al. 2019). These yields are relevant for understanding the early chemical build-up and the initial conditions in the early Galaxy.

Chemical abundances also show variations between old metal-poor stars in different environments such as dwarf galaxies, suggesting that the first stages of enrichment were not uniform. Stars in the nearby dwarf galaxies typically have lower abundances of α - and odd- Z elements, attributed to their slower star formation histories and/or fewer number of high-mass stars overall (Venn et al. 2004; Tolstoy, Hill & Tosi 2009; Nissen & Schuster 2010; McWilliam, Wallerstein & Mottini 2013; Frebel & Norris 2015; Hayes et al. 2018), while significant variations in heavy r -process elements in some dwarf galaxies, and globular clusters, are discussed in terms of contributions from individual compact binary merger events, like GW170817 (e.g. Roederer 2011; Ji et al. 2016; Roederer, Hattori & Valluri 2018a; Ji, Drout & Hansen 2019). In addition, about a third of the $[\text{Fe}/\text{H}] < -2.5$ stars¹ in the Galactic halo show very high enhancements in carbon (the carbon-enhanced metal-poor stars, ‘CEMP’; Yong et al. 2013; Aguado et al. 2019a; also see Kielty et al. 2017; Mardini et al. 2019), discussed as a signature of the earliest chemical enrichment in the Universe. However, at least one ultra-metal-poor star is not carbon enhanced (SDSS J102915+172927, Caffau et al. 2012), and the known metal-poor stars in the Galactic bulge do not show carbon enhancements (Howes et al. 2016; Lamb et al. 2017). Norris et al. (2013) suggest that there are likely multiple chemical enrichment pathways for old metal-poor stars dependent on the star formation environment, and also possibly binary mass-transfer effects (also see discussions by Starkenburg et al. 2014; Arentsen et al. 2019).

The majority of old, metal-poor stars in the Galactic halo are thought to have been accreted from dwarf galaxies at early epochs, based on cosmological hydrodynamical simulations of the Local Group (Ibata, Gilmore & Irwin 1994; Helmi et al. 1999; Ibata et al. 2004; Abadi et al. 2010; Starkenburg et al. 2017a; El-Badry et al. 2018). This is consistent with the high-velocity, eccentric, orbits determined from the exquisite *Gaia* DR2 data (Gaia Collaboration 2018) and spectroscopic radial velocities (RVs) for a majority of the ultra-metal-poor stars (Sestito et al. 2019) and the ultra-faint dwarf galaxies (Simon 2018). Interestingly, many of these orbits are also highly retrograde, similar to the diffuse halo merger remnants, Gaia-Enceladus (Belokurov et al. 2018; Haywood et al. 2018; Helmi et al. 2018; Myeong et al. 2018) and Gaia-Sequoia (Barbá et al. 2019; Myeong et al. 2019). However, some metal-poor stars have been found to have orbits that place them in the Galactic plane (Sestito et al. 2019), even with nearly circular orbits (e.g. SDSS J102915+172927, Caffau et al. 2012). These latter observations challenge the cosmological simulations since metal-poor stars are assumed to be old, and yet the Galactic plane is thought to have

formed only ~ 10 Gyr ago (e.g. Gianninas et al. 2015; Casagrande et al. 2016). Alternatively, Sestito et al. (2019) suggest that these stars may have been brought into the Galaxy from a merger that helped to form the disc.

Progress in this field will require large statistical samples of metal-poor stars in a variety of environments within the Local Group. Unfortunately, metal-poor stars are exceedingly rare and difficult to find, being overwhelmed by the more numerous metal-rich populations in the Galaxy. Examination of the Besançon model of the Galaxy (Robin et al. 2003), which is guided by a theoretical framework for the formation and evolution of the main stellar populations, suggests that a typical halo field has only one in ~ 2000 stars with $[\text{Fe}/\text{H}] < -3$ between $14 < V < 18$ (Youakim et al. 2017). Enormous effort has gone into the discovery and study of extremely, ultra, and hyper metal-poor stars with $[\text{Fe}/\text{H}] < -3.0$, -4.0 , and -5.0 , respectively. Most of the known metal-poor stars have been found in dedicated surveys, such as objective prism surveys (the HK survey and Hamburg-ESO survey, Beers, Preston & Shectman 1992; Christlieb et al. 2002, 2008; Beers & Christlieb 2005; Frebel et al. 2006; Schörck et al. 2009), wide-band photometric surveys (Schlaufman & Casey 2014), and blind spectroscopic surveys, such as the Sloan Digital Sky Survey (SDSS) SEGUE and BOSS surveys (Yanny et al. 2009; Eisenstein et al. 2011; Dawson et al. 2013), and from the Large Sky Area Multi-Object Fibre Spectroscopic Telescope (LAMOST; Cui et al. 2012). According to the SAGA data base (see Suda et al. 2017, and references therein), there are ~ 500 stars with $[\text{Fe}/\text{H}] < -3.0$, though fewer than half have detailed chemical abundances. Recently, narrow-band photometric surveys have shown higher success rates for finding metal-poor stars, particularly SkyMapper (Keller et al. 2007; DaCosta et al. 2019) and the *Pristine* survey (Starkenburg et al. 2017b; Youakim et al. 2017; Aguado et al. 2019a). *Pristine* photometry with follow-up Keck II/DEIMOS spectroscopy has also been used to increase sample sizes and improve the chemodynamical studies of faint satellites (Draco II and Sgr II, Longeard et al. 2018, 2019). At the same time, Simon (2018) has shown that *Gaia* DR2 proper motion cleaning may also be a promising way to find new metal-poor members of ultra-faint dwarf galaxies.

The *Pristine* survey uses a unique narrow-band filter centred on the Ca II H&K spectral lines (‘CaHK’) mounted on MegaPrime/MegaCam at the 3.6-m Canada France Hawaii Telescope (CFHT). When combined with broad-band SDSS *gri* photometry (York et al. 2000), this CaHK filter has been calibrated to find metal-poor candidates with $4200 < T < 6500$ K. The *Pristine* survey has proven successful at predicting metallicities for faint objects ($18 > V > 15$), based on results from medium-resolution spectroscopic follow-up (Youakim et al. 2017; Aguado et al. 2019a). For brighter objects, the success of the *Pristine* calibration is less certain. Caffau et al. (2017) observed 26 bright ($g < 15$) candidates with the FEROS spectrograph at the MPG/ESO 2.2-m telescope, but found only 5 stars with $[\text{Fe}/\text{H}] < -2.0$. It was thought that the selection may be affected by previously unrecognized saturation effects in the SDSS photometry. Thus, Bonifacio et al. (2019) selected bright candidates using a new *Pristine* calibration with the APASS photometry (cf. APASS DR10; Henden 2019); the observations of 40 targets with the SOPHIE spectrograph at Observatoire de Haute Provence found only eight stars with $[\text{Fe}/\text{H}] < -2.0$, and none with $[\text{Fe}/\text{H}] < -3.0$. Until now, the confirmation of the *Pristine* metallicity predictions below $[\text{Fe}/\text{H}] = -3.0$ has only been carried out for one star from high-resolution spectroscopy, *Pristine*.221.8781+09.7844 at $[\text{Fe}/\text{H}] = -4.7$ (1D, LTE) and $V = 16.4$ (Starkenburg et al. 2018).

¹We adopt standard notation, such that $[\text{X}/\text{H}] = \log(\text{X}/\text{H})_{\star} - \log(\text{X}/\text{H})_{\odot}$.

Table 1. Metal-poor targets (115) from the original *Pristine* survey footprint. Herein, 59 stars were selected with a *Pristine* metallicity $[\text{Fe}/\text{H}]_p < -2.5$ and SDSS ($g-i$) and ($g-r$) calibrations with probabilities for both $[\text{Fe}/\text{H}]_{pgi}$ and $[\text{Fe}/\text{H}]_{pgr} < -2.25$ greater than 80 per cent ($d\text{Fe}_p = 1\sigma$). For 10 stars, only the SDSS ($g-r$) calibration was available, as noted. Targets no longer in the *Pristine* catalogue, or with $[\text{Fe}/\text{H}]_p > -2.5$, are also noted. The CaHK and SDSS *ugri* magnitudes are dereddened using the $E(B-V)$ values from the (Schlegel, Finkbeiner & Davis 1998) maps; however, V and I are not dereddened (i.e. observer units). The SDSS colour temperature (T_{SDSS}) averages the dwarf and giant solutions (where $dT = 1\sigma$), and the CFHT program labels are in the comments. Only a sample of the targets is shown here, and the full table is available online.

RA _{SDSS} (deg)	DEC _{SDSS} (deg)	V	I	$E(B-V)$	CaHK ₀	u_0	g_0	r_0	i_0	T_{SDSS} (K)	dT (K)	$[\text{Fe}]_p$	$d\text{Fe}_p$	COMM
High probability for $[\text{Fe}/\text{H}]_p \leq -2.5$ in the <i>Pristine</i> catalogue:														
180.2206	09.5683	14.92	13.99	0.021	15.822	16.439	15.172	14.625	14.392	5202.6	17.6	-2.82	0.02	16BC,17AC
181.2243	07.4160	14.95	14.33	0.015	15.361	15.949	15.044	14.804	14.707	6261.5	5.8	-2.78	0.01	17AC002
181.3464	11.6698	14.18	13.42	0.033	14.782	15.293	14.392	13.841	13.757	5504.8	15.6	-3.82	0.09	16AC031
181.4395	01.6294	14.67	13.66	0.020	15.562	16.345	14.961	14.357	14.078	5011.6	18.5	-3.82	0.09	16BC008

In this paper, we present the analysis of 115 bright ($V < 15$) metal-poor candidates from the *Pristine* survey, calibrated using the original SDSS *gri* photometry and observed at the CFHT with the high-resolution ESPaDOnS spectrograph. Such high-resolution spectra are necessary for detailed chemical abundances, as well as precision RVs for determining the kinematic properties. The power of combining chemical abundances with kinematic properties of stars is the backbone of the field of Galactic Archaeology (e.g. Freeman & Bland-Hawthorn 2002; Venn et al. 2004; Tolstoy et al. 2009; Frebel & Norris 2015). We confirm the success of the *Pristine* survey to find metal-poor stars even at bright magnitudes, determine the chemical abundances for 10 elements, calculate the kinematics of the stars in our sample, and interpret in the context of variations in nucleosynthetic sites, locations, and time-scales. The study of metal-poor old stars is unique to our Local Group, since only here can we resolve individual stars and study these rare targets that guide our understanding of the physics of star formation, supernovae, the early build-up of galaxies, and the epoch of reionization.

2 TARGET SELECTION

Targets were selected from the *Pristine* survey catalogue,² which includes 28 557 bright ($V < 15$) stars in the original ~ 1000 sq. deg² footprint between $180 < \text{RA} < 256^\circ$ and $+00 < \text{Dec} < +16^\circ$ (Starkenburg et al. 2017b; Youakim et al. 2017).

Pristine survey targets were cross-matched with the SDSS photometry to obtain *ugri* broad-band magnitudes used for colour temperature determinations and point-source identification. Additional selection criteria were adopted, as described by Youakim et al. (2017), including the removal of non-star contaminants (based on SDSS and CaHK flags), white dwarf contaminants (removing SDSS $u - g > 0.6$, Lokhorst et al. 2016), variability flags from the Pan-STARRS1 photometry (Hernitschek et al. 2016), and the quality of the SDSS *gri*-band photometry. The SDSS *gri*-band photometry was further used for a colour selection, where $0.25 < (g - i)_o < 1.5$ and $0.15 < (g - r)_o < 1.2$ correspond to the temperature range $4200 \text{ K} < T_{\text{eff}} < 6500 \text{ K}$, covering the tip of the red giant branch and the cooler main sequence to the main-sequence turn-off.

The 115 stars observed at CFHT with the high-resolution ($R \sim 68\,000$) ESPaDOnS spectrograph (Donati et al. 2006) are listed in Table 1 including RA and DEC (from SDSS, in degrees), the dereddened SDSS (*ugri*)₀ and *Pristine*-CaHK₀ magnitudes, the V and I magnitudes [converted from the SDSS photometry using Jordi, Grebel & Ammon (2006) and not dereddened, thus in observer units], and the reddening $E(B - V)$ value. Extinction values are

small for most stars, and we assume that all the extinction is in the foreground, therefore using the Schlegel et al. (1998) extinction maps. A summary of the CFHT ESPaDOnS observing runs that comprise this program is 16AC031 (23 targets), 16AC096 (17 targets), 16BC008 (25 targets), 17AC002 (30 targets), and 18BC018 (25 targets), which is 120 targets, with 5 repeat targets, thus 115 independent objects.

We note that this programme began immediately after the initial *Pristine* survey MegaCam observing runs, and the metallicity calibrations have improved over the course of these spectroscopic follow-up observations (2016A to 2018B). Of the 115 observed stars, 88 remain in the *Pristine* survey catalogue. In Table 1, we have 59 stars with a >80 per cent probability to have $[\text{Fe}/\text{H}] < -2.25$ using both the SDSS $g - r$ and $g - i$ colour calibrations, and with individual metallicity estimates of $[\text{Fe}/\text{H}] < -2.5$. Another 10 stars follow these selections using the SDSS $g - r$ colour alone. Youakim et al. (2017) showed that the SDSS i filter has saturation effects in some fields for stars in our magnitude range that can affect the SDSS $g - i$ selection criterion. An additional 46 stars were observed with ESPaDOnS; however, we now recognize 19 of those to have low probabilities to be metal poor, and 27 are no longer in the *Pristine* survey catalogue (e.g. due to the saturation effects in the SDSS photometry recognized later). Ironically, of those latter 27 stars, one star (Pristine_213.7879+08.4232) does appear to be metal poor, e.g. its Ca II triplet lines are weak and narrow. Possibly the *Pristine* survey selection function is now slightly overly strict; we retained this one metal-poor candidate. Thus, we have observed a total of 70 (59 + 10 + 1) metal-poor candidates selected from the original ~ 1000 sq. deg² footprint of the *Pristine* survey. In total, there are 223 bright stars that meet all of the selection criteria described in this section, thus we have observed 31 per cent (70/223) of these candidates. Both of these distributions are shown in Fig. 1.

The selection criteria used here differ slightly from Youakim et al. (2017) and Aguado et al. (2019a), where stars with probability over 25 per cent in both $g - r$ and $g - i$ were selected for their medium-resolution spectroscopic programme. These lower limits were also adopted by Caffau et al. (2017) and Bonifacio et al. (2019) in their target selections, though using the APASS photometry in the latter paper. We emphasize that our target selections were made without a priori knowledge of the spectroscopic metallicities, other than for a small subset of five stars³ in our final 2018B observing run.

³Five stars had interesting results from our concurrent medium-resolution spectral campaign, and were selected for observations with ESPaDOnS during our final 2018B run. Three were confirmed to be metal poor ($[\text{Fe}/\text{H}] < -2.5$), but two were not ($[\text{Fe}/\text{H}] > -2.0$). If we recalculate our success

²Internal-Catalogue-1802.dat.

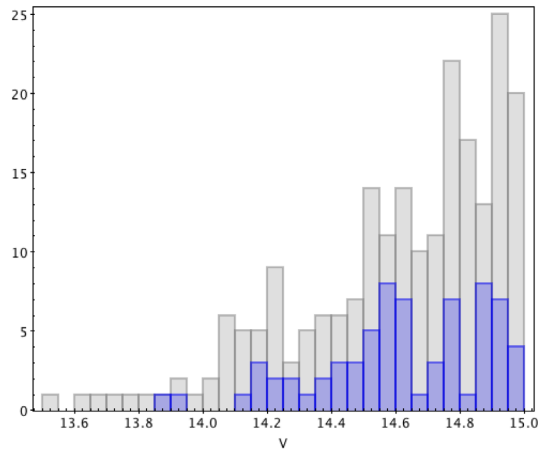


Figure 1. Histogram of the V magnitudes of 223 stars with high probabilities to be metal poor ($[\text{Fe}/\text{H}] < -2.50$) from the $(g-i)$ or $(g-r)$ calibrations in the *Pristine* survey original ~ 1000 sq. deg² footprint (grey bars). The 70 stars observed with CFHT ESPaDOnS that also meet these criteria are overplotted (blue bars).

3 ESPADONS OBSERVATIONS

The CFHT high-resolution spectrograph ESPaDOnS was used between 2016A and 2018B to observe 115 new bright, metal-poor candidates found in the original CFHT-MegaCam survey footprint as part of the *Pristine* survey. ESPaDOnS was used in the ‘star+sky’ mode, providing a high-resolution ($R=68\,000$) spectrum from 400 to 1000 nm, making it possible to determine precision RVs, stellar parameters, and chemical abundances.

Each observation was fully reduced using the Libre-Esprit pipeline.⁴ This included subtraction of a bias and dark frames, flat-fielding for pixel-to-pixel variations, and masking bad pixels. ESPaDOnS records 40 orders, each one of them curved, such that Libre-ESPRIT performs a geometric analysis from the calibration exposures before it performs an optimal extraction. It also corrects for the tilt of the slit, determines the wavelength calibration from a thorium lamp exposure, and applies the heliocentric correction. The ‘star+sky’ mode enables good sky subtraction during the pipeline reductions. The final (combined) spectra were renormalized using an asymmetric k -sigma clipping routine.

As this is an exploratory programme, spectra were collected until signal-to-noise $\text{SNR} > 30$ near 520 nm was reached per target; multiple exposures were coadded for fainter targets to reach this SNR. A full sample spectrum for one metal-poor target is shown in Fig. 2, where it can be seen the SNR worsens at shorter wavelengths. In addition, the red side of the CCD detector in this cross-dispersed Echelle spectrograph is less illuminated than the centre of each order, causing lower SNR in the interorder regions. Overall, this impacts the smoothness of the spectra. Spectral lines in the low-SNR regions were rejected from this analysis. In total, this observing campaign used over 150 h of CFHT ESPaDOnS time.

RVs (see Table 2) were determined by fitting several strong lines per star, and averaging the results from the individual lines together. This method was selected rather than a more rigorous

use of a cross-correlation technique (e.g. IRAF/*fxcorr*) because of slight wavelength solution variations for lines in common between orders and the significant noise in the interorder regions. The typical uncertainty in RV is $\sigma_{\text{RV}} \leq 0.5 \text{ km s}^{-1}$ for lines below 6000 Å. Variations between the RV solutions were noticed between the CaT lines (~ 8500 Å) versus lines in the blue (below 6000 Å), ranging from 0 to 3 km s^{-1} . A similar offset was seen in CFHT ESPaDOnS spectra for CEMP stars by Arentsen et al. (2019), who showed that the RVs derived from lines below 6000 Å provide better agreement with RV standards. Therefore, we did not use any lines above 6000 Å for the RV measurements. The variations for common lines in overlapping orders were small (1–2 pixels, or ≤ 0.8 Å per line); when averaged over several lines (> 10), this intrinsic variation corresponds to $\leq 0.5 \text{ km s}^{-1}$, the RV uncertainty that we adopt for all of our spectra. Multiple observations were spaced over a narrow range in time, so that no RV variability information is available for identifying potential binary systems.

4 SPECTROSCOPIC ANALYSIS

The analysis of stellar spectra requires a comparison with synthetic spectral calculations of the radiative transfer through a model atmosphere. In this paper, we adopt the ATLAS12 (Kurucz 2005) and MARCS (Gustafsson et al. 2008, further expanded by B. Plez) 1D, hydrostatic, plane-parallel models, in local thermodynamic equilibrium. These models are represented by an effective temperature (T_{eff}), surface gravity ($\log g$), and mean metallicity (represented as the iron abundance, $[\text{Fe}/\text{H}]$). The model atmospheres are generated with scaled solar abundances, but increased α element abundances to represent the majority of metal-poor stars in the Galaxy ($[\alpha/\text{Fe}] = 0.0$ to $+0.4$). Microturbulence (ξ) is assumed to scale with gravity, using the scaling relations by Sitnova et al. (2015) and Mashonkina et al. (2017a) for Galactic metal-poor dwarfs and giants, respectively.

Initial stellar parameters (temperature and metallicity) were determined from photometry. A colour temperature was determined from the SDSS *gri* colours and the semi-empirical calibrations from González Hernández & Bonifacio (2009), and metallicity was determined from the SDSS *gri* photometry with the *Pristine* Ca H&K filter, with calibrations described by Starkenburg et al. (2017b). Our targets range in colour temperature ($=T_{\text{SDSS}}$) from 4700 to 6700 K, and have *Pristine* metallicities $[\text{Fe}/\text{H}]_{\text{Pristine}} \lesssim -2.5$; see Table 1.

Sample spectra are shown for six targets: three hot ($T \sim 6500$ K), main-sequence turn-off stars and three cool ($T \sim 4900$ K) red giants in Fig. 4. These spectra are labelled with their target name, temperature (from the Bayesian inference method; see Section 4.1), and metallicity ($[\text{Fe}/\text{H}]_{\text{Q6}}$ from this ‘Quick Six’ analysis; see Section 4.2).

4.1 Stellar parameters using SDSS and *Gaia* DR2 data, and MIST isochrones (‘Bayesian inference’ method)

Improved stellar temperatures and the gravity estimates were determined using a ‘Bayesian inference’ method developed by Sestito et al. (2019). A probability distribution function of the heliocentric distance to each star was inferred by combining the SDSS photometric colours and *Gaia* DR2 parallax data, with stellar isochrones, and a Milky Way stellar density prior. We apply the zero-point offset on the parallax of -0.029 mas recommended by Lindegren et al. (2018), but note that the *Gaia* team have discussed the possibility of spatially correlated parallax errors ranging from

rates without these five stars, then 38 per cent (25/65) are found with $[\text{Fe}/\text{H}] < -2.5$ and 16 per cent (4/25) with $[\text{Fe}/\text{H}] < -3.0$.

⁴Libre-ESPRIT is a self-contained data reduction package developed specifically for reducing the ESPaDOnS Echelle spectropolarimetric data developed by Donati et al. (1997).

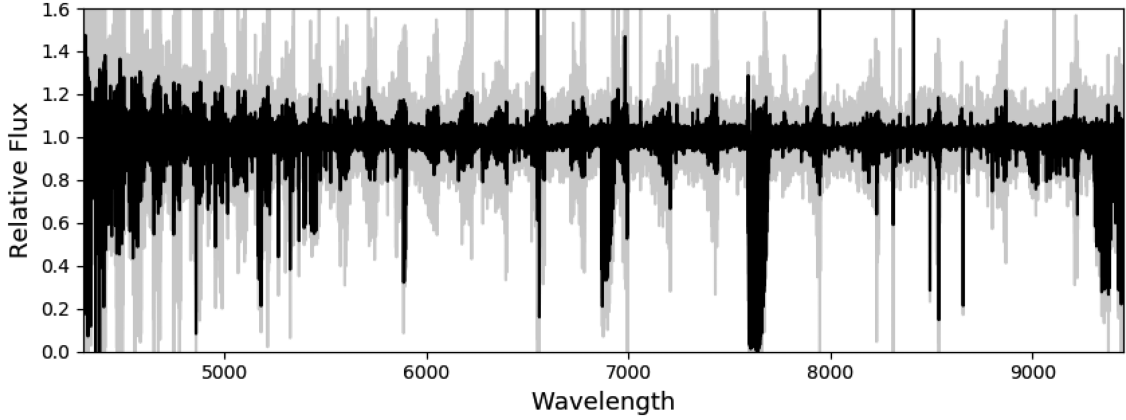


Figure 2. Full CFHT ESPaDOnS spectrum for Pristine-235.1449+08.7464 (grey), and smoothed by a 3-pixel boxcar (black). A signal-to-noise ratio (SNR) =30 near 520 nm was adopted for this exploratory survey, leaving very low SNR and non-smooth continuum on the red side of the detector and therefore in the interorder regions.

Table 2. *Gaia* DR2 parallaxes, and the derived distances (D), temperatures (T), and surface gravities ($\log g$) from the Bayesian inference method (see Section 4.1, assuming $[\text{Fe}/\text{H}]_p$). Corresponding uncertainties are listed as $d\text{par}$, dD , dT , and $d\log g$, respectively. Metallicities are from our ‘Quick Six’ analysis (see Section 4.2) as the individual ion abundances, the weighted average $[\text{Fe}/\text{H}]_{Q6}$, the standard deviation $\sigma_{\text{Fe}Q6}$, and the total number of lines used are noted. For four targets, a second distance ($D2$ in Com) satisfies the Bayesian inference analysis but does not significantly affect the stellar parameters. For four other targets, a dwarf or giant solution has equal probability, and we examine both solutions independently. Stars no longer in the *Pristine* catalogue have been excluded since they are not metal-poor targets, with only one exception (RA=213.7879, DEC=+08.4232, noted as **). The full table is available online.

RA _{SDSS} (deg)	DEC _{SDSS} (deg)	par (mas)	dpar (mas)	D (kpc)	dD (kpc)	T (K)	dT (K)	$\log g$	dlog	RV (km s ⁻¹)	Fe I Q6	Fe II Q6	[Fe/H] Q6	σ_{Fe} Q6	N,Com
High probability for $[\text{Fe}/\text{H}]_p \leq -2.5$:															
180.2206	+09.5683	0.09	0.05	12.08	0.47	5070.6	20.9	1.86	0.05	23.0	4.54	4.31	-3.04	0.18	6
181.2243	+07.4160	0.47	0.05	2.28	0.07	6454.9	99.9	3.81	0.06	-147.0	4.46	4.18	-3.16	0.16	5
181.3464	+11.6698	1.23	0.03	0.60	0.01	6208.3	17.1	4.57	0.01	12.0	7.55	6.86	-0.22	0.15	5
181.4395	+01.6294	0.08	0.05	16.76	0.29	4934.9	8.2	1.41	0.02	206.0	4.83	4.57	-2.76	0.17	6

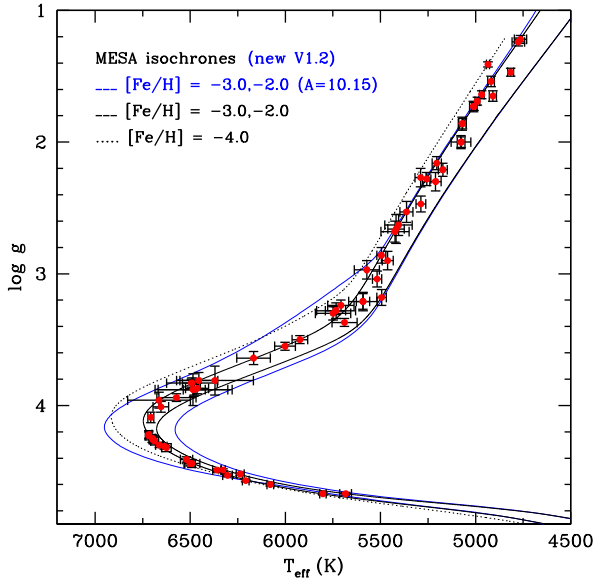


Figure 3. T_{eff} versus $\log g$ for 70 high-probability metal-poor stars selected from the *Pristine* survey. For illustration purposes, the isochrones for a single age of 14.1 Gyr are shown [or $\log(A/\text{yr})=10.15$]. The isochrones used for the stellar parameter estimates are from a previous version of MESA/MIST (shown in black), compared with isochrones from the newer version of MIST (V1.2, shown in blue).

0.1 to 0.01 mas; see discussion by Zinn et al. 2019. Isochrones are from the MESA/MIST library (Paxton et al. 2011; Choi et al. 2016; Dotter 2016), which reach the lowest metallicities ($[\text{Fe}/\text{H}] \leq -4$); see Fig. 3. A flat age prior was assumed between 11 and 14 Gyr [or $\log(A/\text{yr})=10.05$ –10.15], and we adopted the *Pristine* metallicities a priori.

Unique solutions for the stellar parameters were found for 85 of our targets (out of 89 stars; the 88 stars that remain in the *Pristine* survey catalogue after photometric quality cuts, and one star that we have retained; see Section 2). Another four stars have sufficiently large parallax errors that we could not distinguish between the dwarf or giant solutions; both are given in Table 2. It is recognized that determining the distance to a star simply by inverting the parallax measurement can lead to substantial errors, especially when the parallax is small (or even negative), and when there is a relatively large measurement uncertainty (e.g. $\Delta\pi/\pi > 0.1$); see Bailer-Jones et al. (2018). One advantage of this Bayesian inference method is that stars with negative parallax results and stars with very large parallax errors can be placed on to the isochrones and assumed to be distant. In Fig. 5, the Bayesian inferred distances are compared to the *Gaia* DR2 parallax measurements.

For two stars (Pristine_200.5298+08.9768 and Pristine_187.9785+08.7294), the Bayesian inferred distance method seemed to fail, placing these stars in the outer Galactic halo, even though they have relatively large parallax measurements with small uncertainties (0.46 ± 0.04 and 0.74 ± 0.04 mas in the *Gaia* DR2 catalogue), and they are metal rich (e.g. visibly strong Ca II triplet

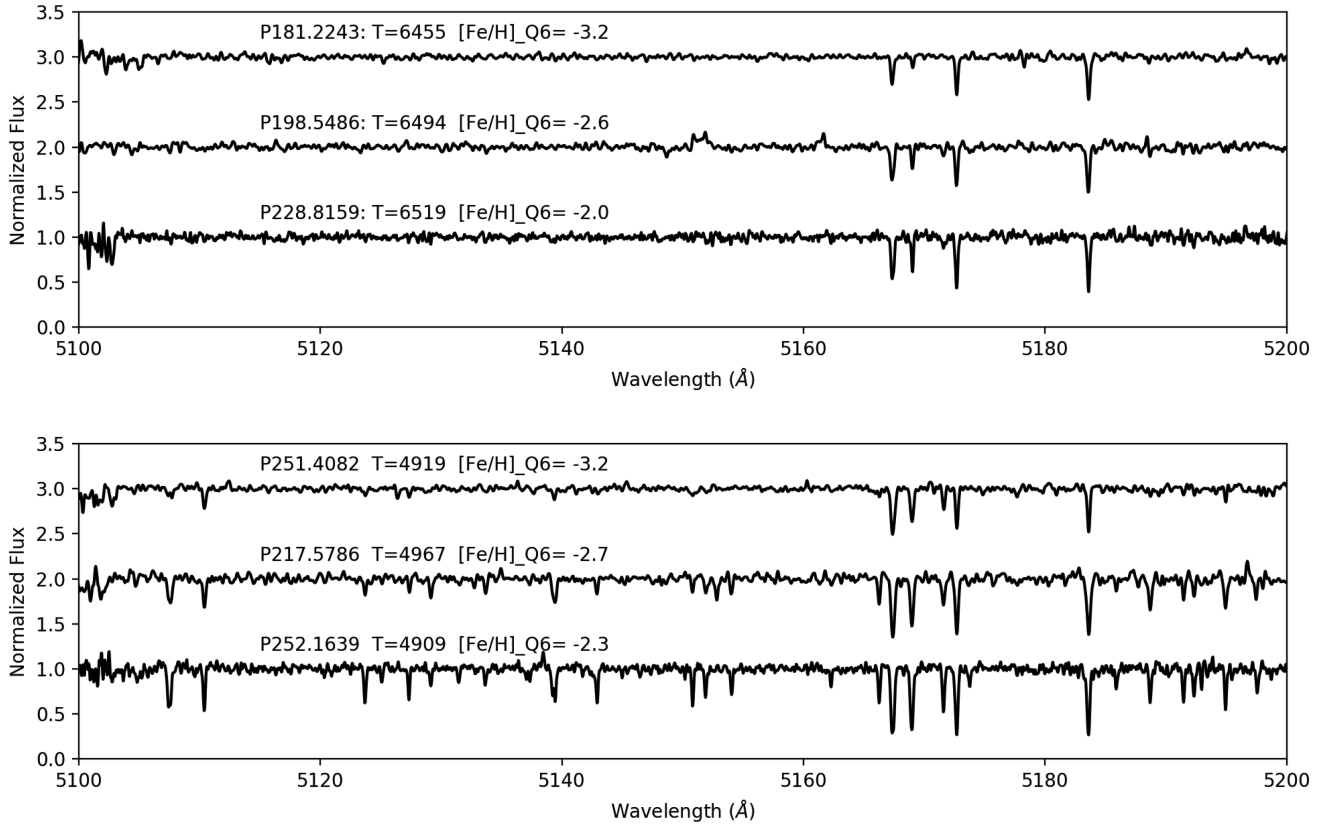


Figure 4. Sample CFHT ESPaDOnS spectra for three hot ($T \sim 6500$ K) main-sequence turn-off stars and three cool ($T \sim 4900$ K) red giants. Each spectrum is labelled with the target name, temperature from the Bayesian inference method, and spectroscopic metallicity from our ‘Quick Six’ analysis.

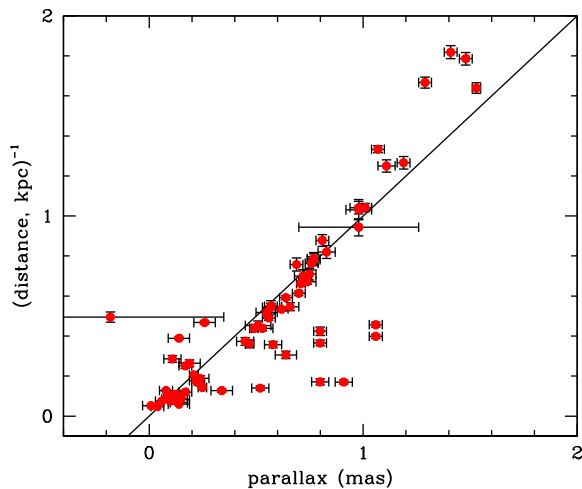


Figure 5. A comparison of the *Gaia* DR2 parallax measurements (with zero-point correction; see the text) and $1/(\text{distance, in kpc})$ from the Bayesian inference method developed by Sestito et al. (2019) for our 70 metal-poor candidates.

lines). Since we had assumed that these stars are metal poor (from their *Pristine* metallicities), then the metal-poor isochrone used to compute their distances was incorrect, and resulted in a poor distance estimate. By adjusting their distances to simply $1/\text{parallax}$ (i.e. not using the metal-poor stellar isochrones), then both of these stars are located closer to the Sun, consistent with the majority of metal-rich stars in the Galaxy. For our main targets, stars that

the *Pristine* survey identifies as metal poor and that are truly metal poor, then this will not be a problem, and we expect that this Bayesian inference method will provide very precise stellar parameters.

4.2 Initial (‘Quick Six’) spectroscopic metallicities

Adopting the stellar parameters from the Bayesian inference method described above (Section 4.1), then a model atmosphere was generated from both the MARCS and ATLAS grids. Elemental abundances were computed using a recent version of the 1D LTE spectrum analysis code MOOG (Snedden 1973; Sobeck et al. 2011).

As an initial spectroscopic metallicity estimate, a subset of six iron lines was selected that are observable in the good SNR regions of the ESPaDOnS spectra: $4 \times \text{Fe I}$ ($\lambda 4957$, $\lambda 5269$, $\lambda 5372$, and $\lambda 5397$) and $2 \times \text{Fe II}$ ($\lambda 4924$ and $\lambda 5018$). These are well known and fairly isolated spectral lines, with good atomic data⁵ and line strengths across the parameter range. The equivalent widths of these six lines were measured using IRAF/*splot*,⁶ measuring both the area

⁵Atomic data for the Fe I lines are from Blackwell, Petford & Shallis (1979) with high precision, or from the laboratory measurements from O’Brian et al. (1991). The Fe II lines have less certain atomic data from Raassen & Uylings (1998); however, a NLTE investigation by Sitnova et al. (2015) showed that these lines have tiny NLTE corrections and yield iron abundances in metal-poor stars within 0.1 dex of all the other Fe I and Fe II lines that they studied. We also note Roederer et al. (2018b) used 3 Fe I and 1 Fe II of these lines in their detailed iron analysis of six warm metal-poor stars.

⁶IRAF is distributed by the National Optical Astronomy Observatories, which is operated by the Association of Universities for Research in

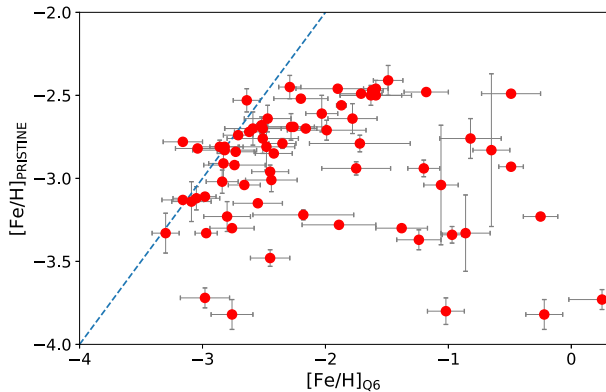


Figure 6. Comparisons of the ‘Quick Six’ $[\text{Fe}/\text{H}]_{\text{Q6}}$ spectral abundances compared with the *Pristine* $[\text{Fe}/\text{H}]_{\text{Pristine}}$ photometric predictions. Clearly, some of the *Pristine* metal-poor candidates are not metal-poor stars.

under the continuum and by fitting a Gaussian profile, comparing the results. We call the average of these six LTE line abundances our ‘Quick Six’ spectroscopic metallicities ($[\text{Fe}/\text{H}]_{\text{Q6}}$), and these are used as an initial test of the *Pristine* metallicity estimates.

Departures from LTE are known to overionize the Fe I atoms due to the impact of the stellar radiation field, particularly in hotter stars and metal-poor giants. These non-LTE (NLTE) effects can be significant in our stellar parameter range, such that NLTE corrections typically reduce the line scatter and improve the Fe I=Fe II ionization balance (Sitnova et al. 2015; Amarsi et al. 2016; Mashonkina et al. 2019). NLTE effects are explored in this ‘Quick Six’ analysis, by comparing the results from Mashonkina et al. (2017a), Mashonkina et al. (2019), and the INSPECT table⁷ (Lind, Bergemann & Asplund 2012; Amarsi et al. 2016). INSPECT provides data for one of the selected lines, Fe I $\lambda 5269$, where the NLTE correction is $\Delta(\text{Fe I}) \leq 0.15$, over our parameter space, where $\text{Fe I(NLTE)} = \text{Fe I(LTE)} + \Delta(\text{Fe I})$. Based on a similar treatment for inelastic collisions (of Fe I with H I), Mashonkina et al. (2017a) predict similar NLTE corrections for the other three Fe I lines ($\lambda 4957$, $\lambda 5372$, and $\lambda 5397$). The largest NLTE corrections [$\Delta(\text{Fe I}) \sim 0.3$] are for stars on the subgiant branch, while main-sequence stars have \sim zero corrections. Recently, Mashonkina et al. (2019) have examined the impact of quantum mechanical rate coefficients for the inelastic collisions, and they find that the latter could be even larger (more positive) in the atmospheres of warm metal-poor stars, but smaller (even negative) in cool metal-poor stars and with a wide variation depending on the specific spectral line. This suggests that the NLTE calculations for Fe I need further study; however, given that these corrections in the literature are smaller than or equal to our measurement errors, then we do not apply the NLTE corrections in this ‘Quick Six’ analysis.

The Fe I and Fe II individual line abundances are averaged together to find $[\text{Fe}/\text{H}]_{\text{Q6}}$ and the standard deviation $\sigma[\text{Fe}/\text{H}]_{\text{Q6}}$. Each of these results and the total number of lines used (≤ 6) are shown in Table 2. From this analysis, we find that several of the *Pristine* metal-poor candidates are not metal poor. A comparison of the $[\text{Fe}/\text{H}]_{\text{Q6}}$ iron abundances to the $[\text{Fe}/\text{H}]_{\text{Pristine}}$ predictions is shown in Fig. 6. These results are similar to the medium-resolution

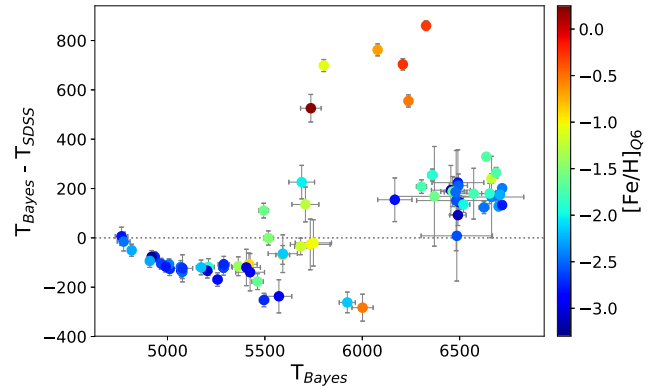


Figure 7. Comparisons of the *Pristine* survey colour temperature (T_{SDSS}) and the effective temperature determined from Bayesian inference method (T_{Bayes}) for our 70 metal-poor candidates. The data points are coloured by their metallicities from our spectroscopic $[\text{Fe}/\text{H}]_{\text{Q6}}$ analysis. As both temperature estimates adopted the *Pristine* photometric metallicity estimates $[\text{Fe}/\text{H}]_{\text{Pristine}}$ a priori, then clearly the metal-rich stars are not well calibrated.

spectral analyses (Youakim et al. 2017; Aguado et al. 2019a), and discussed further in Section 4.5.

4.3 Comparing stellar temperatures

A comparison of stellar temperatures from the Bayesian inference method (Section 4.1) to the SDSS colour temperature (T_{SDSS}) is shown in Fig. 7. T_{SDSS} were the initial temperature estimates calculated using the InfraRed Flux Method,⁸ assuming $[\text{Fe}/\text{H}] = -2.5$, and based on the SDSS ($g - i$) photometry. An average of the dwarf and giant solutions was used. For 10 stars, their ($g - i$) colours are unreliable because of saturation flags, and we adopt the relation based on the ($g - r$) colours from Ivezić et al. (2008). With this relation, a 200 K offset was applied to move from $[\text{Fe}/\text{H}] = -0.5$ to -2 . Thus, we expect these values of T_{SDSS} to be an oversimplification, and are not surprised by the comparisons in Fig. 7, which are colour coded by the ‘Quick Six’ metallicities $[\text{Fe}/\text{H}]_{\text{Q6}}$.

Ignoring the metal-rich stars, then there is still a systematic offset between these methods for the metal-poor stars: the T_{SDSS} colour temperatures are too hot by ~ 150 K for stars between $T = 4700$ and 5700 K, but they are too cool by ~ 200 K for stars with $T > 6000$ K. This offset is similar to the uncertainties in the Bayesian inference method temperatures (T_{Bayes}) for most stars, where σT_{Bayes} ranges from ~ 10 to 200 K (Table 2). The very small colour temperature errors $dT_{\text{SDSS}} \lesssim 10$ K in Table 1 are based on the difference between the dwarf/giant solutions, and are not realistic uncertainties.

4.4 Comparing gravity and Fe I=Fe II

Ionization balance has traditionally been used as an indicator of surface gravity in a classical model atmosphere analysis. Therefore, we compare the $\log g$ values from the Bayesian inference method (Section 4.1) to the difference in the $[\text{Fe I}]$ and $[\text{Fe II}]$ abundances, in Fig. 8. This figure is colour coded by the ‘Quick Six’ spectroscopic metallicities ($[\text{Fe}/\text{H}]_{\text{Q6}}$). For the metal-poor stars, the majority of our stars show Fe I=Fe II to within 2σ of the measurement errors,

Astronomy, Inc. (AURA) under cooperative agreement with the National Science Foundation.

⁷Non-LTE data obtained from the INSPECTdata base (version 1.0), available at <http://inspect-stars.com>.

⁸IRFM; see <https://www.sdss.org/dr12/spectro/sspp.irfm/>.

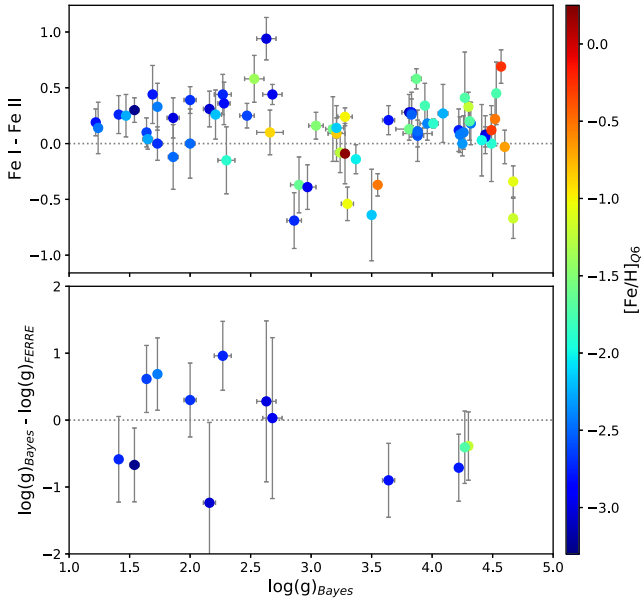


Figure 8. Comparisons of the surface gravities and iron ionization balance estimates for our 70 metal-poor candidates from the *Pristine* survey (top panel), and comparisons of our surface gravities versus those from the FERRE analysis of medium-resolution spectra (Aguado et al. 2019a) for 13 stars in common. The uncertainties in the gravities from FERRE can be quite large for the metal-poor stars due to a lack of suitable spectral signatures. The data points are coloured by their metallicities from our spectroscopic $[\text{Fe}/\text{H}]_{\text{Q6}}$ analysis.

with a mean offset of $[\text{Fe I}] - [\text{Fe II}] = +0.2$. The measurement errors are calculated as the line-weighted average of Fe I and Fe II.

For stars with poor agreement between iron ionization states, the cause cannot be due to neglected NLTE effects, which appear to increase the Fe I abundance even further (see in Section 4.2). The offset is primarily seen in the cooler stars in our sample that are on the red giant branch (with lower gravities). For these stars, the NLTE corrections are expected to be small $[\Delta(\text{Fe I}) \lesssim 0.15]$. For stars closer to the main-sequence turn-off, the NLTE corrections can be larger; however, the offset between the Fe I and Fe II abundances seems smaller for those stars in our results. Therefore, the source of ionization equilibrium offsets is not yet clear.

For the metal-rich stars, we expect the surface gravities to be unreliable since the photometric *Pristine* metallicities $[\text{Fe}/\text{H}]_{\text{Pristine}}$ were assumed a priori in the Bayesian inference method. We do not investigate the metal-rich stars beyond our ‘Quick Six’ analysis.

4.5 Comparisons with medium-resolution spectroscopic analyses (FERRE)

A simultaneous *Pristine* survey programme has been carried out for fainter stars ($15 < V < 17$) with medium-resolution ($R \sim 1800$) spectroscopy at the 2.4-m Isaac Newton Telescope (INT), 4.2-m William Herschel Telescope, and 3.6-m New Technology Telescope (Aguado et al. 2019a). These spectra have been observed with uniform spectral wavelength coverage, 360–550 nm, and analysed using the ASSET synthetic spectral grid (Koesterke, Allende Prieto & Lambert 2008). Both the observed and the synthetic spectra have been continuum normalized with the same functions, and the χ^2 minimization algorithm FERRE (Allende Prieto et al. 2006) is applied to derive the stellar parameters (temperature, gravity, metallicity, and carbonicity).

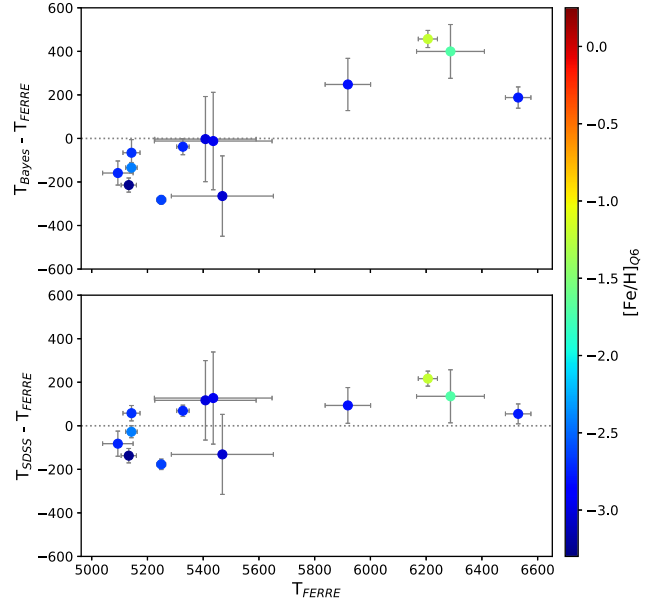


Figure 9. Temperature comparisons for 13 stars in common between the Bayesian inference analysis of our CFHT ESPaDOnS spectra and the FERRE analysis of medium-resolution spectra (top panel, Aguado et al. 2019a). The temperature offsets are slightly smaller when compared with the *Pristine* colour temperatures (T_{SDSS} , bottom panel).

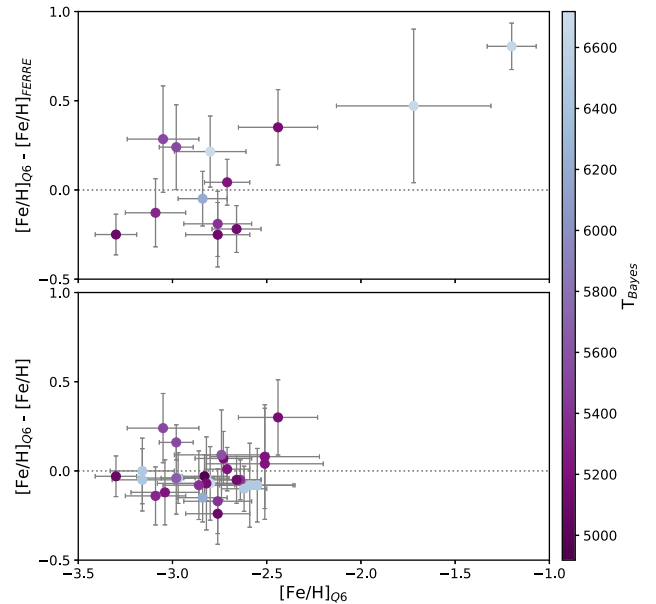


Figure 10. Metallicity comparisons for 13 stars in common between the $[\text{Fe}/\text{H}]_{\text{Q6}}$ analysis of our CFHT ESPaDOnS spectra and the FERRE analysis of medium-resolution spectra (top panel, Aguado et al. 2019a). $[\text{Fe}/\text{H}]_{\text{Q6}}$ values are also compared to the improved $[\text{Fe}/\text{H}]$ values for our 28 very metal poor stars, which include more lines of both Fe I and Fe II. The errors in the bottom panel are dominated by the ‘Quick Six’ $\sigma[\text{Fe}/\text{H}]_{\text{Q6}}$ analysis.

The most recent analysis of the medium-resolution spectroscopic data includes 946 stars (Aguado et al. 2019a), where 13 of those stars are also in our sample of 70 high-probability metal-poor stars (recall that only 5 were observed at the INT first, and did not affect our target selections). In Figs 8, 9, and 10, the surface gravities, temperatures, and metallicities are compared between the two analyses for

the 13 stars in common. The large differences in gravity are from the *systematic* errors in the medium-resolution FERRE analysis. While the FERRE analysis struggles with precision gravities, both methods are still able to break the dwarf-giant degeneracies sufficiently.

There is a clear relationship between the temperatures such that those determined from isochrones in the Bayesian inference method are cooler by ~ 200 K near 5000 K and hotter by ~ 500 K near 6700 K compared to the FERRE temperatures. These offsets are slightly smaller when compared with the SDSS colour temperatures T_{SDSS} . These temperature differences correlate with small-to-moderate metallicity offsets ($\Delta[\text{Fe}/\text{H}] \leq 0.3$) for stars cooler than 6000 K, whereas two of the hotter stars show larger metallicity offsets, $\Delta[\text{Fe}/\text{H}] \sim 0.5$. In summary, this analysis adopts the stellar parameters from the Bayesian inference method, and finds that the hot stars are hotter and less metal poor than the results from the medium-resolution FERRE analysis.

5 NEW STARS WITH $[\text{Fe}/\text{H}] \leq -2.5$

We have identified 28 new metal-poor stars, with a spectroscopic metallicity $[\text{Fe}/\text{H}]_{\text{Q6}} \leq -2.5$, and where both $[\text{Fe I}/\text{H}]$ and $[\text{Fe II}/\text{H}]$ are below -2.5 dex (with the exception of Pristine_198.5486+11.4123, with $[\text{Fe I}/\text{H}] = -2.42$, which we retain because of its interesting orbit, discussed below). In this section, a more complete LTE, 1D model atmosphere analysis is carried out for a larger set of spectral lines and chemical elements (see Table 3).

As a comparison star, a spectrum of HD 122563 from the CFHT archive was analysed using the same methods as for the *Pristine* survey targets. Its metallicity is adopted from the literature, i.e. $[\text{Fe}/\text{H}] = -2.7 \pm 0.1$ (see Collet et al. 2018, and references therein), and our methods using its SDSS colours and *Gaia* DR2 parallax measurements yield stellar parameters that are in good agreement with the literature: $T_{\text{eff}} = 4625 \pm 50$ K and $\log g = 1.6 \pm 0.1$. Microturbulence (ξ) was set to 2.0 km s^{-1} using the relationship with gravity from Mashonkina et al. (2017a).

For all 28 *Pristine* survey stars and HD122563, we identify and measure as many clean spectral lines as possible for a detailed abundance analysis, including more lines of Fe I and Fe II for higher precision iron abundances (than from the $[\text{Fe}/\text{H}]_{\text{Q6}}$ analysis). Starting with the spectral line list from Norris et al. (2017), spectral features were identified and measured using DAOSpec (Stetson & Pancino 2008), and frequently checked by measuring the area under the continuum using IRAF/*splot*. Atomic data were updated when appropriate by comparing to the *linemake* atomic and molecular line data base.⁹ Abundance results from the model atmosphere analysis are compared to the solar (photospheric) abundances from Asplund et al. (2009).

5.1 Iron-group elements

The 28 new very metal poor stars were initially identified from their $[\text{Fe}/\text{H}]_{\text{Q6}}$ abundances in Table 2.

The iron abundances have been recalculated from 2–86 lines of Fe I and 2–6 lines of Fe II; see Table 4. A 3σ minimum equivalent

width was used to calculate an upper limit for Fe II for one star. The line-to-line scatter in the Fe I abundances ranges from $\sigma(\text{Fe I}) = 0.12$ to 0.24, even when only a small number of lines were measured. This is noteworthy because when other elements have <4 lines, we adopt the larger of $\sigma(X)$ or $\sigma(\text{Fe I})/\sqrt{N_X}$ as a better representation of their line scatter.

These extended iron-line measurements and abundances are not used to redetermine the spectroscopic stellar parameters for three reasons: (1) low sensitivity to the precise metallicity in the Bayesian inference method for the confirmed metal-poor stars, (2) insufficient number of lines of Fe II (and often Fe I) for a fully independent analysis, and (3) the SNR of our CFHT ESPaDOnS spectra (≤ 30) is such that individual measurements of weak lines remain somewhat uncertain. The total iron abundance $[\text{Fe}/\text{H}]$ is calculated as a weighted mean of Fe I and Fe II, and the total error $\delta[\text{Fe}/\text{H}]$ as $\sigma([\text{Fe}/\text{H}])/(N_{\text{Fe I}} + N_{\text{Fe II}})^{1/2}$. These iron abundances are shown in Fig. 11 (top panel), where the errorbars include the systematic errors from the stellar parameter uncertainties added in quadrature (see Section 5.5, though the systematic errors tend to be much smaller).

There is good to fair agreement between Fe I and Fe II, such that $[\text{Fe I}] - [\text{Fe II}]$ ranges from ~ -0.2 to $+0.2$. There is a median offset $\sim +0.2$ for the sample, which is *not* due to ignoring NLTE corrections (see the discussion in Section 4.2). This may be due to the lack of the Fe II lines in our metal-poor-stars spectra for robust measurements, but another possibility is a systematic gravity uncertainty $\Delta \log g \sim 0.5$. High-resolution spectra at bluer wavelengths (4000 \AA) would provide more lines of Fe II to test this in the future. We also examine the slopes in the Fe I line abundances versus excitation potential (χ , in eV) to test our temperature estimates. A meaningful slope could be measured when $N(\text{Fe I}) > 15$ and $\Delta \chi > 3 \text{ eV}$, and all slopes were found to be relatively flat, $<0.1 \text{ dex eV}^{-1}$. This gives us more confidence in the fidelity of the temperatures T_{Bayes} , and thereby the Bayesian inference method for calculating stellar parameters and uncertainties.

The other iron-group elements (Cr and Ni, listed in Table 4) are in good agreement with $[\text{Fe}/\text{H}]$, and/or other Galactic halo stars at similar metallicities; see Fig. 11. Cr is determined from 1–3 lines of Cr I (5206.0, 5208.4, and 5409.8 \AA); only the spectrum of Pristine_245.8356+13.8777 had sufficient SNR at blue wavelengths in that the lines at 4254.3, 4274.8, and 4289.7 \AA could also be observed. $[\text{Cr}/\text{Fe}]$ is subsolar in metal-poor stars, suggested as a NLTE effect (Bergemann & Cescutti 2010). Ni is determined from 1–2 lines of Ni I (5035.4 and 5476.9 \AA). Three additional lines were available in the high-SNR spectrum of HD 122563 (5080.5, 6643.6, and 6767.8 \AA). The $[\text{Ni}/\text{Fe}]$ results are within 1σ of the solar ratio, similar to other Galactic halo stars.

5.2 α -elements

The α -element abundances (Mg and Ca) in the 28 new very metal poor stars are listed in Table 5. Upper limits are determined for some stars by computing 3σ minimum equivalent widths. The α -elements form through hydrostatic H- and He-core burning stages, though some Ca can also form later during SN Ia events. Because of these different nucleosynthetic sites, the $[\text{Mg}/\text{Ca}]$ ratio need not scale together at all metallicities, as seen in some dwarf galaxies such as the Carina and Sextans dwarf galaxies (e.g. Venn et al. 2012; Jablonka et al. 2015; Norris et al. 2017), also the unusual star cluster NGC 2419 (Cohen & Kirby 2012). We also include our discussion of Ti in this section even though it does not form with the α -elements. The dominant isotope ^{48}Ti forms primarily through Si-burning in massive stars (e.g. Woosley, Heger & Weaver 2002),

⁹*linemake* contains laboratory atomic data (transition probabilities, hyperfine and isotopic substructures) published by the Wisconsin Atomic Physics and the Old Dominion Molecular Physics groups. These lists and accompanying line list assembly software have been developed by C. Sneden and are curated by V. Placco at <https://github.com/vmplacco/linemake>.

Table 3. Line list from Norris et al. (2017) with atomic data updates from *linemake* (see the text). Equivalent width measurements are provided per star (labelled by RA_{SDSS} only). The full table is available online.

Elem	Wavel (Å)	χ (eV)	$\log(gf)$	180.2206 (mÅ)	181.2243 (mÅ)	181.4395 (mÅ)	181.6849 (mÅ)	189.9449 (mÅ)	193.8390 (mÅ)	196.3755 (mÅ)	198.3755 (mÅ)	201.8711 (mÅ)
Mg I	5172.684	2.710	−0.40	165.2	105.0	181.3	56.0	94.2	185.7	160.4	109.5	72.3
Mg I	5183.604	2.715	−0.18	161.6	124.9	214.4	86.0	112.2	201.7	186.5	139.0	90.7
Fe II	4923.922	2.891	−1.21	65.7	25.3	92.9	–	28.3	101.0	108.1	39.6	–
Fe II	5018.435	2.891	−1.35	79.7	–	104.4	–	35.9	94.0	88.6	53.5	–

Table 4. Iron-group and heavy element abundances in the new 28 metal-poor stars (labelled by RA_{SDSS}), and our analysis of HD122563. [Fe/H] is the weighted mean of Fe I and Fe II, and $\delta([Fe/H]) = \sigma([Fe/H])/\sqrt{N_{Fe I} + N_{Fe II}}$.

RA _{SDSS}	[Fe/H] $\pm \delta$	$\log(Fe I) \pm \sigma$ (N)	$\log(Fe II) \pm \sigma$ (N)	[Cr/Fe] $\pm \sigma$ (N)	[Ni/Fe] $\pm \sigma$ (N)	[Y/Fe] $\pm \sigma$ (N)	[Ba/Fe] $\pm \sigma$ (N)
180.2206	−2.92 \pm 0.03	4.60 \pm 0.18 (49)	4.45 \pm 0.27 (4)	−0.21 \pm 0.13 (2)	−0.05 \pm 0.18 (1)	<+0.49	−1.02 \pm 0.18 (1)
181.2243	−3.11 \pm 0.07	4.50 \pm 0.17 (4)	4.17 \pm 0.14 (2)	–	–	<+1.85	<+1.37
181.4395	−2.52 \pm 0.02	4.99 \pm 0.18 (86)	4.80 \pm 0.26 (5)	−0.37 \pm 0.11 (3)	+0.03 \pm 0.13 (2)	<−0.12	−1.13 \pm 0.24 (2)
183.6849	−3.16 \pm 0.07	4.38 \pm 0.24 (2)	4.30 \pm 0.01 (2)	–	–	<+2.33	<+1.88
189.9449	−2.78 \pm 0.04	4.77 \pm 0.12 (8)	4.50 \pm 0.21 (2)	–	–	<+1.70	<+0.93
193.8390	−2.80 \pm 0.02	4.71 \pm 0.21 (81)	4.49 \pm 0.13 (5)	−0.49 \pm 0.12 (3)	−0.24 \pm 0.21 (1)	<+0.02	−1.58 \pm 0.21 (1)
196.3755	−2.80 \pm 0.02	4.70 \pm 0.19 (61)	4.72 \pm 0.16 (3)	−0.17 \pm 0.14 (2)	−0.21 \pm 0.19 (1)	<+0.3	<−0.56
198.5486	−2.47 \pm 0.05	5.08 \pm 0.16 (9)	4.80 \pm 0.29 (2)	+0.04 \pm 0.11 (2)	<+0.45	<+1.23	<+0.39
201.8711	−2.93 \pm 0.11	4.57 \pm 0.15 (2)	<4.71	–	–	<+2.10	<+1.65
203.2831	−2.74 \pm 0.02	4.77 \pm 0.19 (59)	4.55 \pm 0.15 (4)	−0.27 \pm 0.11 (3)	−0.19 \pm 0.19 (1)	<+0.01	−0.76 \pm 0.23 (3)
204.9008	−2.73 \pm 0.08	4.84 \pm 0.18 (3)	4.66 \pm 0.26 (2)	–	–	<+1.89	<+1.40
208.0798	−2.94 \pm 0.03	4.53 \pm 0.14 (20)	4.83 \pm 0.26 (2)	−0.35 \pm 0.10 (2)	<+0.16	<+1.15	<+0.57
210.0166	−2.59 \pm 0.02	4.92 \pm 0.18 (64)	4.75 \pm 0.13 (4)	−0.20 \pm 0.13 (2)	−0.17 \pm 0.18 (1)	<+0.51	+0.74 \pm 0.20 (4)
213.7879	−2.59 \pm 0.02	4.93 \pm 0.18 (61)	4.55 \pm 0.17 (3)	−0.09 \pm 0.11 (3)	+0.11 \pm 0.18 (1)	<+0.43	−0.36 \pm 0.14 (2)
214.5556	−2.51 \pm 0.05	5.01 \pm 0.15 (10)	4.88 \pm 0.35 (2)	<+0.07	<+0.69	+1.48 \pm 0.11 (2)	+1.77 \pm 0.22 (4)
217.5786	−2.61 \pm 0.02	4.88 \pm 0.18 (79)	4.94 \pm 0.18 (6)	−0.11 \pm 0.16 (4)	−0.04 \pm 0.18 (1)	+0.16 \pm 0.13 (2)	+0.02 \pm 0.18 (3)
229.1219	−2.52 \pm 0.04	5.02 \pm 0.12 (8)	4.84 \pm 0.17 (2)	+0.16 \pm 0.12 (1)	–	<+1.59	<+0.44
233.5730	−2.75 \pm 0.02	4.77 \pm 0.20 (75)	4.42 \pm 0.28 (3)	−0.25 \pm 0.12 (3)	–	<+0.23	−0.15 \pm 0.32 (3)
235.1449	−2.69 \pm 0.04	4.85 \pm 0.15 (16)	4.52 \pm 0.13 (2)	<−0.16	–	<+1.41	+0.13 \pm 0.15 (1)
237.8246	−3.29 \pm 0.04	4.28 \pm 0.15 (13)	3.73 \pm 0.04 (2)	<−0.32	<+0.50	<+1.29	+0.61 \pm 0.34 (2)
240.4216	−2.95 \pm 0.03	4.56 \pm 0.20 (41)	4.20 \pm 0.22 (2)	−0.35 \pm 0.14 (2)	−0.19 \pm 0.20 (1)	<+0.64	+0.53 \pm 0.29 (4)
245.5747	−3.14 \pm 0.04	4.37 \pm 0.20 (18)	4.25 \pm 0.09 (2)	<−0.30	<+0.38	<+1.14	<+0.52
245.8356	−2.78 \pm 0.03	4.73 \pm 0.21 (52)	4.60 \pm 0.25 (4)	−0.41 \pm 0.16 (5)	+0.18 \pm 0.21 (1)	+0.73 \pm 0.21 (1)	−0.51 \pm 0.12 (3)
248.4959	−2.59 \pm 0.02	4.91 \pm 0.17 (74)	4.90 \pm 0.31 (5)	−0.26 \pm 0.10 (3)	−0.04 \pm 0.12 (2)	<+0.16	−0.18 \pm 0.10 (3)
250.6963	−2.55 \pm 0.03	4.95 \pm 0.20 (62)	4.95 \pm 0.28 (4)	−0.43 \pm 0.12 (3)	+0.07 \pm 0.14 (2)	<+0.18	−0.03 \pm 0.16 (3)
251.4082	−3.27 \pm 0.03	4.23 \pm 0.18 (31)	4.19 \pm 0.33 (3)	<−0.17	–	<+0.65	−0.73 \pm 0.18 (1)
253.8582	−2.72 \pm 0.02	4.80 \pm 0.21 (65)	4.54 \pm 0.07 (4)	−0.15 \pm 0.14 (2)	−0.13 \pm 0.21 (1)	<+0.35	−0.51 \pm 0.20 (3)
255.5555	−2.83 \pm 0.03	4.64 \pm 0.18 (22)	4.99 \pm 0.10 (2)	<−0.08	<−0.08	<+0.97	+0.35 \pm 0.10 (3)
HD122563	−2.76 \pm 0.01	4.73 \pm 0.15 (98)	4.86 \pm 0.16 (5)	−0.39 \pm 0.08 (3)	+0.05 \pm 0.10 (5)	−0.15 \pm 0.11 (2)	−0.77 \pm 0.08 (3)

and yet it seems to scale with other α -elements in metal-poor stars in the Galaxy.

Mg is determined from 2–3 lines (5172.7, 5183.6, and 5528.4 Å), and a fourth line (4703.0 Å) was measurable in one star (Pristine_245.8356+13.8777). In Fig. 12, a larger scatter can be seen in the [Mg/Fe] results, though this is similar to the Galactic comparison stars. One star shows subsolar [Mg/Fe] by more than 1σ (Pristine_251.4082+12.3657). Another star has high [Mg/Fe] \sim +0.6, validated from all the three Mg I lines (Pristine_181.2243+07.4160), also shown in Fig. 13.

The calcium abundances are determined from 1–9 lines of Ca I. The [Ca/Fe] abundances are in good agreement with each other, and with the Galactic comparison stars, as seen in Fig. 12. The same star with low [Mg/Fe] (Pristine_251.4082+12.3657) also has a very low [Ca/Fe] upper limit. This star is discussed further in Section 6.2.

Titanium has been determined from 1–9 lines of Ti I and 2–11 lines of Ti II. When both are unavailable, upper limits are determined from the two Ti II lines (which provide stronger constraints than the

Ti I features). In Fig. 12, the unweighted average results of [Ti I/Fe] and [Ti II/Fe] are shown.

NLTE corrections have not been incorporated for Mg, Ca, or Ti because they tend to be small to negligible ($\Delta \leq 0.1$ dex) according to the INSPECT data base (for Mg I) and Mashonkina, Sitnova & Belyaev (2017b, for Ca I). For Ti I, three lines (4981.7, 4991.1, and 4999.5 Å) are available in the INSPECT data base, which suggests large corrections $\Delta \sim$ +0.5 dex. However, NLTE corrections for the same lines from Sitnova, Mashonkina & Ryabchikova (2016), using a model atom that includes important high excitation levels of Ti I, are significantly smaller, $\Delta \sim$ +0.2 dex. NLTE corrections should be included, but most of our stars have Ti I \sim Ti II to within 1σ (our measurement errors) in LTE. Therefore, for this analysis, where the maximum SNR per star is ≤ 30 , we do not include the small NLTE corrections, and note that the good agreement with the Galactic comparison stars and Ti ionization balance furthers our confidence in the stellar parameters from the Bayesian inference method.

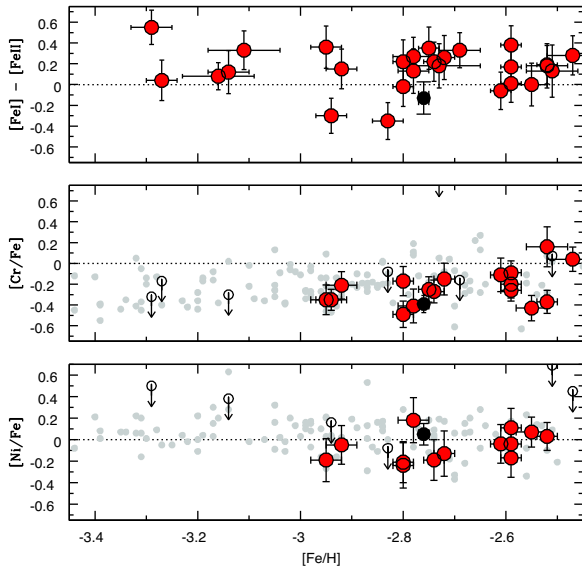


Figure 11. Iron-group (Fe, Cr, and Ni) abundances and upper limits in our 28 new very metal poor stars ($[\text{Fe}/\text{H}] < -2.5$, red points). Analysis results of the CFHT ESPaDOnS spectrum for the standard star HD 122563 are included (black point). Errorbars are the measurement errors and systematic errors combined in quadrature. Galactic comparison stars are included from the homogeneous analysis by Yong et al. (2013, small grey points).

No oxygen abundances or upper limits were determined since the $[\text{O I}]$ 6300 and 6363 Å lines are weak and in a region that is poorly cleaned of telluric contaminants.

5.3 Odd elements

Odd elements, Na and Sc, are listed in Table 5. These have different nucleosynthetic sources and are not related to one another. We also include a comment on Li upper limits at the end of this section.

In metal-poor stars, sodium typically forms with the α -elements during core-collapse SN. On the other hand, scandium forms in the iron core of a massive star with a yield that strongly depends on the proton-to-neutron ratio (Y_e), and it is very sensitive to neutrino processes (e.g. Woosley et al. 2002; Curtis et al. 2019).

Sodium abundances are initially from the LTE analysis of the Na I D lines (5889.9 and 5895.9 Å), which unfortunately can be strong, therefore sensitive to microturbulence in a 1D LTE analysis, and also contaminated by interstellar Na. Furthermore, since they originate from the Na I ground state, they are subject to NLTE effects. NLTE corrections are similar between the INSPECT data base and Mashonkina et al. (2017c); $[\text{Na}/\text{H}]_{\text{NLTE}} = [\text{Na}/\text{H}]_{\text{LTE}} + \Delta\text{Na}$, where $\Delta\text{Na} = (-0.1) - (-0.6)$ dex. The Na I subordinate line (5688.2 Å) could only be used for upper limit estimates at the SNR of our spectra.

Despite the large NLTE corrections, four stars were found with initially very high Na I abundances (Pristine_251.4082+12.3657, Pristine_193.8390+11.4150, Pristine_217.5786+14.0379, and Pristine_250.6963+08.3743, in order of decreasing metallicity). These four stars also have the lowest RVs in our sample (-5 , $+4$, -16 , and -4 km s $^{-1}$, in order of decreasing metallicity), and we suggest they are contaminated by the interstellar Na lines. To test this, their Na I D line shapes were compared with other spectral lines in the same stars and found to be slightly broader (occasionally, the line core is even split); their Na I D line shapes are also broader than similar stars with higher RVs (where the

interstellar lines are often seen offset from the stellar lines). Thus, in Fig. 14, the highest Na abundances are noted as upper limits only since they are most likely blended, and for the other stars the NLTE-corrected Na abundances are shown.

Sc II has been measured from 1–3 lines (5031.0, 5526.8, and 5657.9 Å) in five metal-poor *Pristine* stars, and the comparison star HD 122563, and upper limits were determined in the others. With an odd number of nucleons, this species undergoes strong hyperfine splitting, which affects line formation through de-saturation. The HFS corrections were found to be small (<0.1). Upper limits have also been determined for Sc II in most of the other new metal-poor stars. Upper limits were examined for Mn I as well, but did not provide interesting constraints.

Lastly, we mention Li in this section. Estimates from the Li I 6707 Å line provide upper limits that do not provide meaningful constraints, i.e. the upper limits are above the standard big bang nucleosynthesis value of $A(\text{Li}) = 2.7$ (e.g. from WMAP, Spergel et al. 2003). Only two stars (Pristine_229.1219+00.9089 and Pristine_237.8246+10.1426) have 3σ equivalent width (35 mÅ) upper limits of $A(\text{Li}) \leq 2.2$, which is similar to most metal-poor stars that lie on (or below) the Spite Plateau (e.g. see Bonifacio et al. 2018; Aguado et al. 2019b).

5.4 Heavy elements

Abundances for the neutron-capture elements Y and Ba in the 28 new very metal poor stars are listed in Table 4. Up to four lines of Ba II (4554.0, 5853.7, 6141.7, and 6496.9 Å) and two lines of Y II (4883.7 and 4990.1 Å) could be measured. Unfortunately, no lines or useful upper limits for Eu are available in our CFHT spectra. When no lines were observable, we determined upper limits from 3σ minimum equivalent width estimates. Hyperfine splitting and the isotopic splitting have been included in the Ba analysis. Most stars have $[\text{Ba}/\text{Fe}]$ in good agreement with the Galactic comparison stars.

All the six lines were measured in only one star near $[\text{Fe}/\text{H}] = -2.5$ (Pristine_214.5555+07.4670). This star is enriched in both Y and Ba, and we identify it as an r-process-rich star. Without Eu, it cannot be further classified as r-I or r-II (Christlieb et al. 2004; Sakari et al. 2018b). Studies of r-process-rich stars have found a nearly identical main r-process pattern (from barium, $A=56$, to hafnium, $A=72$) in all types of stars, in all environments, and with variations only between the lightest and heaviest elements (see Roederer et al. 2010; Hill et al. 2017; Sakari et al. 2018a, and references therein). No other elements stand out in this star; however, as one of the hotter turn-off stars in our sample, there are not many other features or elements to analyse at the SNR of our spectra.

Two more stars show $[\text{Ba}/\text{Fe}] \gtrsim +0.5$ (Pristine_237.8246+10.1426 and Pristine_210.0166+14.6289). These lie above the typical $[\text{Ba}/\text{Fe}]$ values found in the Galactic halo metal-poor stars by Roederer et al. (2014), and their results are securely derived from 2–4 Ba II line measurements. However, no Y II lines were observed in either (and the Y II upper limits do not provide useful constraints). The two may be moderately r-process-enriched stars.

Possibly of greater interest are the two most Ba-poor stars (Pristine_181.4395+01.6294 and Pristine_193.8390+11.4150). Low Ba is very unusual at their metallicities when compared with the other Galactic halo stars, as seen in Fig. 15. This composition is similar to stars in the Segue 1 and Hercules ultra-faint dwarf (UFD) galaxies (Koch et al. 2013; Frebel, Simon & Kirby 2014). In Segue 1, the Ba-poor stars were discussed as representative of inhomogeneous enrichment by a single (or few) supernova event, and therefore

Table 5. Light element abundances in the new 28 metal-poor stars (labelled by RA_{SDSS}), and our analysis of HD122563. When the number of lines $N_X < 4$ for species X, then $\sigma(X) = \sigma(\text{Fe I})/\sqrt{N_X}$.

RA _{SDSS}	[Na/Fe] $\pm \sigma$ (N)	[Mg/Fe] $\pm \sigma$ (N)	[Ca/Fe] $\pm \sigma$ (N)	[Sc/Fe] $\pm \sigma$ (N)	[TiI/Fe] $\pm \sigma$ (N)	[TiII/Fe] $\pm \sigma$ (N)
180.2206	+0.39 \pm 0.13 (2)	+0.30 \pm 0.11 (3)	+0.35 \pm 0.10 (4)	–	+0.22 \pm 0.13 (2)	+0.28 \pm 0.11 (3)
181.2243	–0.23 \pm 0.17 (1)	+0.67 \pm 0.13 (2)	<+0.94	–	–	<+1.23
181.4395	+0.07 \pm 0.13 (2)	+0.26 \pm 0.11 (3)	+0.42 \pm 0.19 (9)	–0.15 \pm 0.11 (3)	+0.16 \pm 0.19 (9)	+0.19 \pm 0.16 (8)
183.6849	–0.18 \pm 0.17 (2)	+0.13 \pm 0.14 (3)	<+1.01	–	–	<+1.88
189.9449	+0.01 \pm 0.08 (2)	+0.17 \pm 0.08 (2)	<+0.65	–	–	<+0.92
193.8390	<+1.17	+0.37 \pm 0.12 (3)	+0.33 \pm 0.14 (8)	+0.08 \pm 0.12 (3)	+0.09 \pm 0.12 (8)	+0.17 \pm 0.18 (8)
196.3755	+0.22 \pm 0.13 (2)	+0.29 \pm 0.11 (3)	+0.45 \pm 0.24 (7)	–	+0.43 \pm 0.25 (4)	+0.28 \pm 0.19 (4)
198.5486	+0.24 \pm 0.11 (2)	+0.25 \pm 0.09 (3)	+0.53 \pm 0.16 (1)	<+0.97	–	<+0.71
201.8711	–0.12 \pm 0.11 (2)	–0.05 \pm 0.11 (2)	<+1.16	–	–	<+1.59
203.2831	+0.66 \pm 0.13 (2)	+0.02 \pm 0.13 (2)	+0.21 \pm 0.11 (3)	–	+0.43 \pm 0.06 (6)	+0.50 \pm 0.10 (5)
204.9008	–0.15 \pm 0.18 (1)	–0.12 \pm 0.13 (2)	<+0.96	–	–	<+1.36
208.0798	+0.26 \pm 0.10 (2)	+0.09 \pm 0.08 (3)	+0.45 \pm 0.14 (1)	–	–	<+0.78
210.0166	+0.06 \pm 0.13 (2)	+0.18 \pm 0.11 (3)	+0.36 \pm 0.28 (4)	<+0.44	+0.37 \pm 0.11 (3)	+0.12 \pm 0.13 (2)
213.7879	–0.12 \pm 0.13 (2)	+0.33 \pm 0.11 (3)	+0.44 \pm 0.09 (4)	<+0.26	+0.45 \pm 0.24 (7)	+0.45 \pm 0.13 (2)
214.5556	+0.02 \pm 0.12 (2)	+0.36 \pm 0.09 (3)	<+0.82	<+1.11	–	<+0.96
217.5786	<+1.14	+0.22 \pm 0.11 (3)	+0.55 \pm 0.24 (6)	+0.09 \pm 0.13 (2)	+0.23 \pm 0.12 (5)	+0.55 \pm 0.16 (10)
229.1219	–0.13 \pm 0.09 (2)	+0.22 \pm 0.09 (2)	–	–	+1.26 \pm 0.12 (1)	+1.44 \pm 0.12 (1)
233.5730	+0.65 \pm 0.14 (2)	+0.24 \pm 0.12 (3)	+0.39 \pm 0.32 (5)	<+0.10	+0.24 \pm 0.15 (4)	+0.28 \pm 0.12 (3)
235.1449	–0.26 \pm 0.11 (2)	+0.09 \pm 0.11 (2)	<+0.67	<+1.16	–	<+0.94
237.8246	+0.00 \pm 0.11 (2)	+0.04 \pm 0.11 (2)	<+0.88	<+1.12	–	<+0.89
240.4216	+0.14 \pm 0.14 (2)	+0.14 \pm 0.12 (3)	+0.31 \pm 0.12 (3)	<+0.54	+0.44 \pm 0.14 (2)	+0.52 \pm 0.14 (2)
245.5747	–0.17 \pm 0.14 (2)	+0.14 \pm 0.14 (2)	<+0.96	<+0.99	...	<+0.75
245.8356	+0.67 \pm 0.15 (2)	+0.29 \pm 0.11 (4)	+0.66 \pm 0.22 (6)	+0.30 \pm 0.15 (2)	+0.64 \pm 0.15 (2)	+0.46 \pm 0.25 (11)
248.4959	+0.39 \pm 0.13 (2)	+0.14 \pm 0.10 (3)	+0.35 \pm 0.17 (7)	<+0.07	+0.48 \pm 0.28 (4)	+0.36 \pm 0.18 (5)
250.6963	<+1.71	+0.11 \pm 0.12 (3)	+0.57 \pm 0.38 (8)	+0.03 \pm 0.20 (1)	+0.40 \pm 0.24 (6)	+0.39 \pm 0.12 (8)
251.4082	<+1.61	–0.20 \pm 0.13 (2)	<+0.11	<+0.52	–	<+0.28
253.8582	+0.12 \pm 0.15 (2)	+0.23 \pm 0.12 (3)	+0.27 \pm 0.20 (4)	<+0.20	+0.39 \pm 0.24 (4)	+0.37 \pm 0.18 (5)
255.5555	+0.76 \pm 0.13 (2)	+0.29 \pm 0.11 (3)	+0.46 \pm 0.10 (3)	<+0.78	–	<+0.88
HD122563	+0.21 \pm 0.11 (2)	+0.18 \pm 0.09 (3)	+0.32 \pm 0.14 (8)	+0.19 \pm 0.11 (2)	+0.07 \pm 0.05 (9)	+0.46 \pm 0.08 (9)

possibly related to first stars. Higher SNR data for these two stars are warranted in order to test this hypothesis.

Finally, one star (Pristine.245.8356+13.8777) shows a high Y II abundance, but a normal Ba II abundance. A similar star was recently studied by Caffau et al. (2019, J0222–0313), where the authors show it is a CEMP-s star, having undergone mass transfer in a binary system with an Asymptotic Giant Branch (AGB) star. However, they also suggest that the AGB star in this system may have undergone a proton ingestion event just before the mass transfer that produced an enhancement in only the first s-process peak elements.

5.5 Abundance uncertainties

Total uncertainties in the chemical abundances are a combination of the measurement uncertainties and systematic errors in the stellar parameters, added in quadrature. For the measurement errors, when fewer than four lines are available for an element X, then we adopt the larger of $\sigma(X)$ or $\sigma(\text{Fe I})/\sqrt{N_X}$. Since the Fe I lines are measured across the entire spectrum and over a range of equivalent widths and excitation potentials, then this assumes that $\sigma(\text{Fe I})$ captures the minimum measurement quality of our spectra. For the systematic errors, due to uncertainties in the stellar parameters, we determine the impact of the 1σ changes in temperature, gravity, and metallicity listed in Table 2.

A sample of the systematic uncertainties for three stars that cover the parameter space of this sample is shown in Table 7. It can be seen that temperature tends to be the dominant systematic error in the analysis of most elements. While we could further investigate the

impact of the final metallicities [Fe/H] and uncertainties $\sigma([\text{Fe/H}])$ through iterations in the Bayesian inference method on the model atmospheres parameters, we did not; the only stars that we follow up in detail are those that did prove to be very metal poor, therefore the impact of adjusting for the final metallicities on the other stellar parameters is very small.

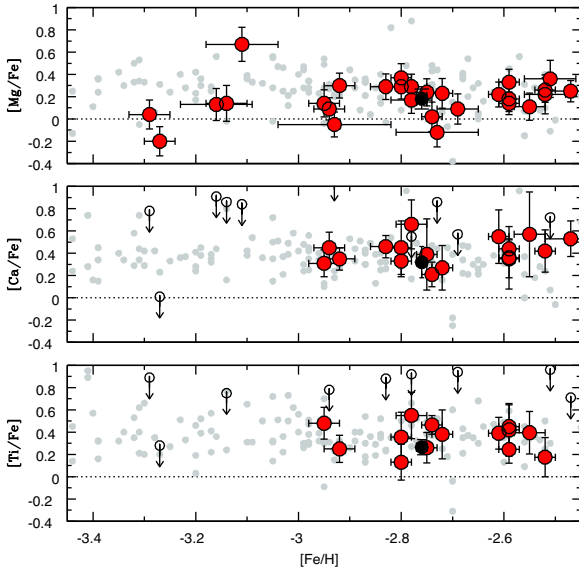
6 DISCUSSION

A total of 70 (out of 115) bright, metal-poor candidates have been observed with the CFHT ESPaDOnS spectrograph from the original footprint (~ 1000 sq. deg) of the *Pristine* survey. These targets were selected to have a high probability for $[\text{Fe/H}]_{\text{Pristine}} < -2.5$, when the *Pristine* CaHK filter was calibrated with the SDSS $g-i$ and $g-r$ colours (60 stars), or only the SDSS $g-r$ colour alone (10 stars). We carry out a model atmosphere analysis by adopting stellar parameters determined from a Bayesian inference method that uses the SDSS colours, *Gaia* DR2 parallaxes, and MESA/MIST isochrones, assuming the initial *Pristine* survey metallicities. Out of these 70 selected stars, we have found 28 to indeed have low metallicities, $[\text{Fe/H}] \leq -2.5$ (40 per cent). The *Pristine* survey had also predicted that 27 stars would have $[\text{Fe/H}] \leq -3.0$, and 5 were found (19 per cent). Of the 42 remaining stars ($-2.5 < [\text{Fe/H}]_{Q6} < +0.25$), there are no obvious relationships with any other stellar parameters (e.g. see Fig. 16), although we notice that all of the candidates on the upper red giant branch were successfully selected and confirmed to be metal-poor stars.

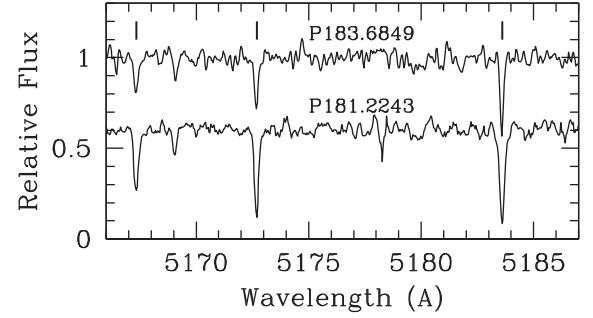
The selections made in this paper differ from those used by Youakim et al. (2017) and Aguado et al. (2019a) (see Section 2)

Table 6. Total systematic errors (dX) per element species (X) due to the stellar parameters (T , $\log g$, $[\text{Fe}/\text{H}]$), added in quadrature, where dT and dlog are from Table 2 and $\delta[\text{Fe}/\text{H}]$ is from Table 4. Stars are labelled by RA_{SDSS}.

RA _{SDSS}	dFe I	dFe II	dNa	dMg	dCa	dSc	dTi I	dTi II	dCr I	dNi I	dY II	dBa II
180.2206	0.03	0.02	0.03	0.02	0.01	—	0.02	0.02	0.02	0.02	—	0.02
181.2243	0.09	0.03	0.07	0.08	—	—	—	—	—	—	—	—
181.4395	0.01	0.01	0.01	0.01	0.01	0.01	0.01	0.01	0.01	0.01	—	—
183.6849	0.04	0.01	0.03	0.03	—	—	—	—	—	—	—	—
189.9449	0.12	0.02	0.09	0.09	—	—	—	—	—	—	—	—
193.8390	0.04	0.01	0.05	0.04	0.03	0.01	0.05	0.01	0.04	0.04	—	—
196.3755	0.02	0.01	0.02	0.02	0.01	—	0.03	0.01	0.02	0.02	—	—
198.5486	0.04	0.01	0.03	0.03	0.03	—	—	—	0.04	—	—	—
201.8711	0.03	—	0.02	0.02	—	—	—	—	—	—	—	—
203.2831	0.01	0.01	0.02	0.02	0.01	—	0.02	0.01	0.01	0.01	—	0.01
204.9008	0.01	0.01	0.01	0.01	—	—	—	—	—	—	—	—
208.0798	0.07	0.03	0.07	0.06	0.05	—	—	—	0.06	—	—	—
210.0166	0.03	0.02	0.03	0.03	0.02	—	0.03	0.02	0.03	0.03	—	0.03
213.7879	0.03	0.03	0.03	0.04	0.02	—	0.03	0.03	0.03	0.03	—	0.03
214.5556	0.17	0.03	0.13	0.14	—	—	—	—	—	—	0.09	0.15
217.5786	0.01	0.01	0.02	0.02	0.01	0.01	0.02	0.01	0.01	0.01	—	—
229.1219	0.16	0.05	0.12	0.15	—	—	0.15	0.06	0.15	—	0.08	—
233.5730	0.02	0.01	0.02	0.02	0.01	—	0.02	0.01	0.02	—	—	0.01
235.1449	0.08	0.02	0.06	0.08	—	—	—	—	—	—	—	0.06
237.8246	0.09	0.03	0.07	0.07	—	—	—	—	—	—	—	0.06
240.4216	0.03	0.02	0.02	0.02	0.02	—	0.03	0.02	0.03	0.03	—	0.02
245.5747	0.08	0.03	0.07	0.08	—	—	—	—	—	—	—	—
245.8356	0.02	0.02	0.03	0.02	0.02	0.02	0.03	0.02	0.03	0.02	—	—
248.4959	0.02	0.01	0.03	0.02	0.01	—	0.02	0.02	0.02	0.02	—	0.02
250.6963	0.02	0.01	0.04	0.02	0.02	0.02	0.02	0.02	0.02	0.02	—	—
251.4082	0.02	0.01	0.03	0.02	—	—	—	—	—	—	—	0.02
253.8582	0.06	0.02	0.06	0.06	0.04	—	0.06	0.03	0.06	0.06	—	0.04
255.5555	0.03	0.02	0.03	0.03	0.02	—	—	—	—	—	—	0.02
HD122563	0.03	0.02	0.04	0.03	0.02	0.01	0.04	0.01	0.03	0.03	—	—

**Figure 12.** Mg, Ca, and Ti abundances and upper limits in the 28 new metal-poor stars ($[\text{Fe}/\text{H}] < -2.5$); the symbols are the same as in Fig. 11.

being far more strict in the metal-poor probability cuts. Furthermore, about 1/3 of the targets in this programme were observed before the selection criteria were finalized. Nevertheless, our success rates are very similar to the results from the medium-resolution surveys. We do not reproduce the (lower) success rates for bright stars seen in earlier *Pristine* survey papers (Caffau et al. 2017; Bonifacio

**Figure 13.** The spectrum of the Mg *1b* lines in the Mg strong star, P181.2243. This star is compared to Pristine_183.6849+04.8619, which has very similar stellar parameters [$T \sim 6450$, $\log(g) \sim 4$, and $[\text{Fe}/\text{H}] \sim -3.2$], but is Mg normal.

et al. 2019), partially due to our improved (more strict) selection criteria, partially due to differences between the SDSS and APASS photometry, and possibly due to the larger number of stars in this sample.

In the remainder of this discussion, we examine the kinematic and orbital properties of the 70 metal-poor candidates in this paper, and correlate those with their chemical abundances. We caution that these calculations and our interpretations are highly dependent on the accuracy of the adopted Milky Way potential (described in the next section). For example, our orbit integrations do not account for effects like the Galactic bar, which can significantly influence halo star orbits (e.g. Hattori, Erkal & Sanders 2016; Price-Whelan et al. 2016; Pearson, Price-Whelan & Johnston 2017).

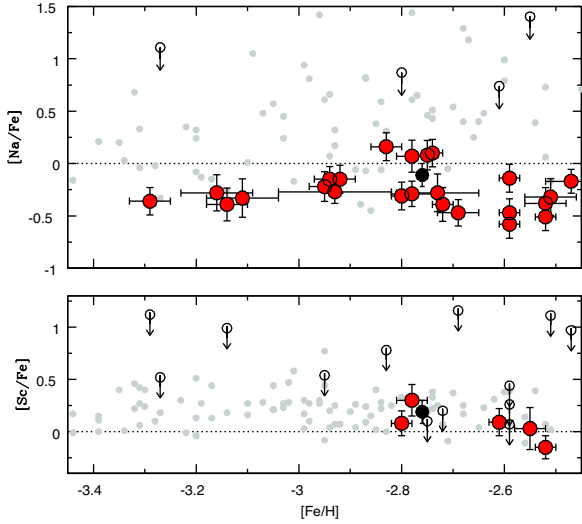


Figure 14. Na and Sc abundances and upper limits in the 28 new metal-poor stars ($[\text{Fe}/\text{H}] < -2.5$); the symbols are the same as in Fig. 11. NLTE corrections for Na have been applied from INSPECT (Amarsi et al. 2016).

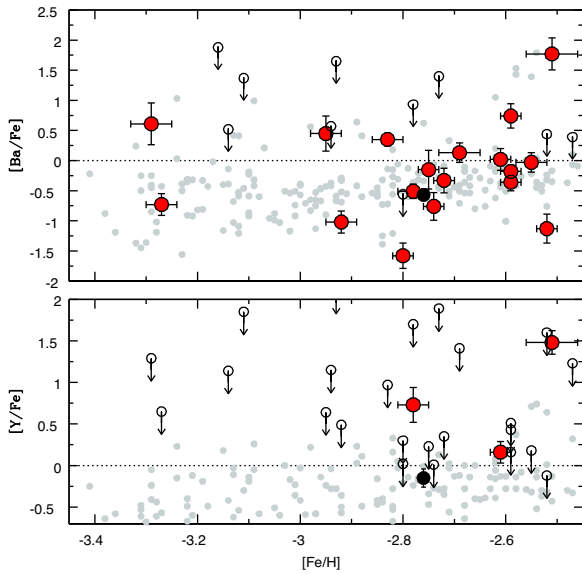


Figure 15. Ba and Y abundances and upper limits in the 28 new metal-poor stars ($[\text{Fe}/\text{H}] < -2.5$); the symbols are the same as in Fig. 11 with the exception of the Galactic comparison stars from Roederer et al. (2014, small grey points). We identify one star near $[\text{Fe}/\text{H}] = -2.5$ (Pristine_214.5556+07.4669) as an r-process-rich star, significantly enriched in both Y and Ba.

6.1 Kinematics and orbits

Galactocentric velocities (U , V , and W) are calculated for each star from their Galactic Cartesian coordinates (X , Y , Z) following the methods of Bird et al. (2019). The distance between the Sun and the Galactic centre is taken to be 8.0 kpc, the Local Standard of Rest circular velocity is $V_{\text{circ}} = 239 \text{ km s}^{-1}$, and the peculiar motion of the Sun is ($U_0 = 11.10 \text{ km s}^{-1}$; $V_0 + V_{\text{circ}} = 251.24 \text{ km s}^{-1}$; $W_0 = 7.25 \text{ km s}^{-1}$), as described in Schönrich, Binney & Dehnen (2010). The sign of U_0 is changed so that U is positive towards the Galactic anticentre. Errors in these velocities are propagated from the uncertainties in proper motion, RVs, and distance by calculating

the mean dispersions from 1000 Monte Carlo realizations, and selecting from a Gaussian distribution in each of the original quantities.

With the distances from the Bayesian inference analysis,¹⁰ precision RVs from our high-resolution spectra, and proper motions from the *Gaia* DR2 data base, then the orbital parameters for the sample are calculated using the Galpy package (Bovy 2015). The *MWPotential14* is adopted, a Milky Way gravitational potential composed of a power law, exponentially cut-off bulge, Miyamoto Nagai Potential disc, and Navarro, Frenk & White (1997) dark matter halo. A more massive halo is chosen following Sestito et al. (2019), with a mass of $1.2 \times 10^{12} M_{\odot}$, which is more compatible with the value from Bland-Hawthorn & Gerhard (2016).

The UVW velocities for the 70 highly probable metal-poor stars in this sample are given in Table A1 (see Appendix A). The Toomre diagram for these objects is shown in Fig. 17, colour coded by the $[\text{Fe}/\text{H}]_{\text{Q6}}$ metallicities. Most of the metal-poor stars in our sample have halo-like velocities, as expected for their metallicities. One very metal poor star (Pristine_183.6849+04.8619, discussed below) appears to have disc-like dynamics.

6.2 Orbit analyses

To investigate the relationships between the chemical and kinematic properties of the stars in our sample, we examine their maximum excursions. This includes the apocentric and pericentric distances (R_{apo} and R_{peri}), perpendicular distance from the Galactic plane (Z_{max}), and eccentricity (e) of the derived orbits; see Table A1.

In Fig. 18, stars with $R_{\text{apo}} < 15 \text{ kpc}$ and $Z_{\text{max}} < 3 \text{ kpc}$ are considered to be confined to the Galactic plane (16 stars), while stars with $R_{\text{apo}} > 30 \text{ kpc}$ are considered to be members of the outer halo (10 stars). The outer halo star Pristine_251.4082+12.3657 has the largest R_{apo} distance in our sample, with a highly eccentric orbit, and it is one of the most metal-poor stars ($[\text{Fe}/\text{H}] = -3.3$), with low abundances of $[\text{Mg}/\text{Fe}]$ and $[\text{Ca}/\text{Fe}]$ (see Fig. 12), and also low $[\text{Ba}/\text{Fe}]$. This chemical signature is typical of stars in or accreted from the nearby dwarf galaxies. Alternatively, it may have been accreted from an *ultra*-faint dwarf galaxy, since its chemistry is also similar to the unique stars CS 29498–043 and CS 29249–037 (Aoki et al. 2002; Depagne et al. 2002), both near $[\text{Fe}/\text{H}] = -4$. These stars have been proposed to be second-generation stars, which formed from gas enriched by a massive Population III first star, exploding as a fall-back supernova (see also Frebel et al. 2019), and as such they would have formed in a now accreted *ultra*-faint dwarf galaxy.

In Fig. 19, only stars with $R_{\text{apo}} < 30 \text{ kpc}$ are shown. Clearly, most of the stars confined to the Galactic plane ($Z_{\text{max}} < 3 \text{ kpc}$) are the relatively metal-rich (interloping) stars in our sample. However, one of the most metal-poor stars (Pristine_183.6849+04.8619, $[\text{Fe}/\text{H}] = -3.1$) is also confined to the Galactic plane with a nearly circular orbit ($e=0.3$). This was also seen in the Toomre diagram (Fig. 17). A detailed view of the orbit of this star is shown in Fig. 20. Most of the spectral lines in this star are weak and so we were unable to determine many elemental abundances, only $[\text{Mg}/\text{Fe}] = +0.13$ (± 0.14) and $[\text{Na}/\text{Fe}] = -0.18$ (± 0.17), which are both quite low for a typical halo metal-poor star. Ultra-metal-poor stars ($[\text{Fe}/\text{H}] < -4$) have been found on similar quasi-circular and planar orbits by

¹⁰For three stars, we reverted back to distances from their $1/\text{parallax}$ values based on unrealistic outer halo distances and other orbital properties. Two of these stars were discussed at the end of Section 4.1, and a third star is discussed in Appendix A.

Table 7. Samples of systematic errors per star (labelled by RA_{SDSS}) per elemental species, which were added in quadrature per star in Table 6. We note that if $\sigma_{Fe I}$ is used instead of $\sigma[Fe/H]$, then the errors due to metallicity remain negligible.

RA_{SDSS}	Parameter	$X \pm dX$	dFe I	dFe II	dNa I	dMg I	dCa I	dSc II	dTi I	dTi II	dCr I	dNi I	dY II	dBa II
193.8390	Temperature	4764 ± 32 K	0.04	-0.01	0.05	0.03	0.03	0.01	0.05	0.01	0.04	0.04	-	-
193.8390	Log g	1.22 ± 0.03	0.00	0.01	-0.01	-0.01	0.00	0.01	0.00	0.01	0.00	0.00	-	-
193.8390	[Fe/H]	-2.80 ± 0.02	0.00	0.00	0.00	0.00	0.00	0.00	0.00	0.00	0.00	0.00	-	-
213.7879	Temperature	5289 ± 29 K	0.03	0.00	0.03	0.03	0.02	-	0.03	0.01	0.03	0.03	-	0.02
213.7879	Log g	2.27 ± 0.07	0.00	0.03	0.00	-0.02	0.00	-	0.00	0.02	0.00	0.00	-	0.02
213.7879	[Fe/H]	-2.59 ± 0.02	0.00	0.00	0.00	0.00	0.00	-	0.00	0.00	0.00	0.00	-	0.00
214.5556	Temperature	6482 ± 203 K	0.17	0.02	0.13	0.14	-	-	-	-	-	-	0.09	0.15
214.5556	Log g	3.88 ± 0.05	0.00	0.02	0.00	-0.01	-	-	-	-	-	-	0.02	0.01
214.5556	[Fe/H]	-2.50 ± 0.05	0.00	0.00	0.00	0.00	-	-	-	-	-	-	0.00	0.00

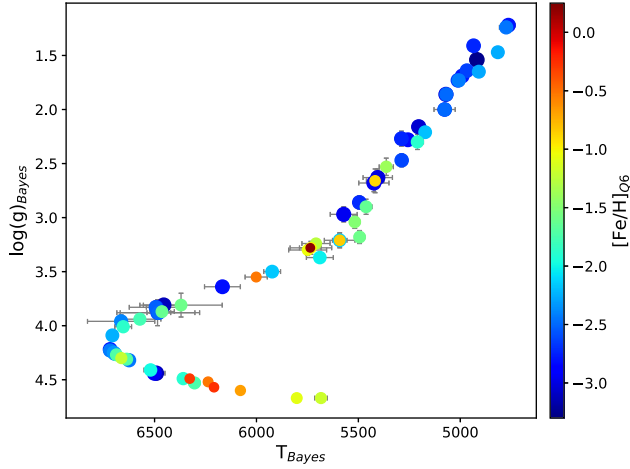


Figure 16. The HRD for the 70 metal-poor candidates in the *Pristine* survey, colour coded by their ‘Quick Six’ metallicities $[Fe/H]_{Q6}$ as determined from our high-resolution CFHT ESPaDOnS spectrum and Bayesian inference analysis. Stars that are not very metal poor, with $[Fe/H] > -2.0$, are located over all stellar parameters.

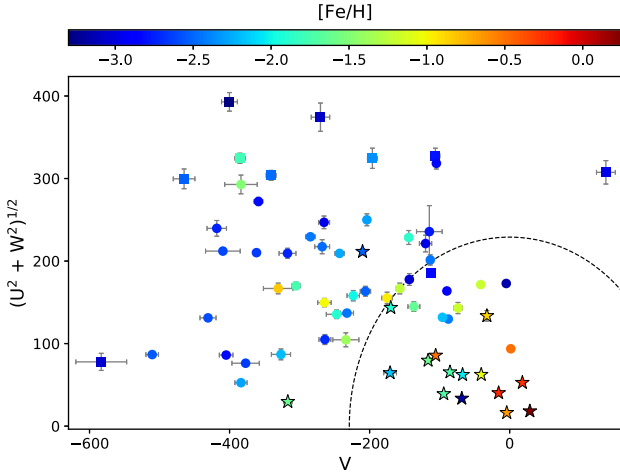


Figure 17. Toomre diagram for the 70 highly probable metal-poor stars in our *Pristine* survey sample. The dashed line represents stars potentially with disc dynamics ($V_{circ} = 239$ km s $^{-1}$). The symbols are the same as in Fig. 18.

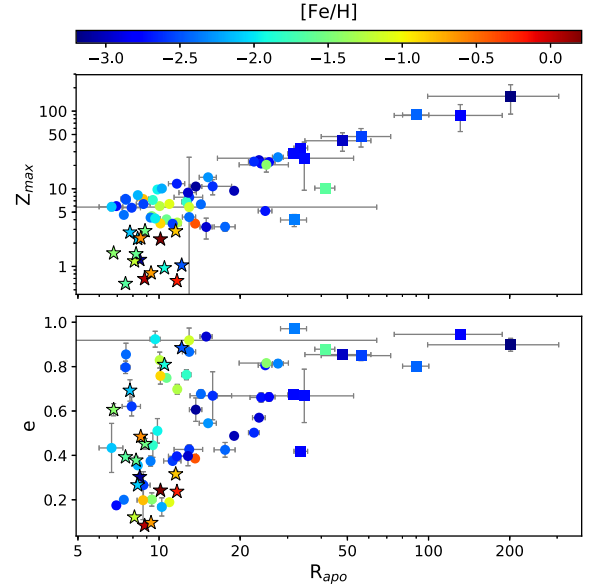


Figure 18. Perpendicular distance from the Galactic plane (Z_{max}) and eccentricity (e) of the orbits versus apocentric distance (R_{apo}) for the 70 high-probability metal-poor stars in this paper. For targets with $R_{apo} < 15$ and $Z_{max} < 3$ kpc, we adopt ‘star’ symbols, for $R_{apo} < 30$ kpc we adopt circle symbols, and when $R_{apo} > 30$ kpc we adopt square symbols. All targets are colour coded by their $[Fe/H]_{Q6}$ metallicities.

Sestito et al. (2019), and interpreted as stars that may have been brought in during the early merger phase of the building blocks of the proto-MW that eventually formed the disc.

Several (8) stars in our sample have orbits that take them deep into the Galactic bulge ($R_{peri} < 1$ kpc). All of these stars are on highly radial orbits ($e > 0.8$), and two are very metal poor; Pristine_250.6963+08.3743 at $[Fe/H] = -2.55 \pm 0.03$, and Pristine_201.8710+07.1810 at $[Fe/H] = -2.93 \pm 0.11$. While the former star shows typical halo abundances in $[(Mg, Ca, Ti)/Fe] = +0.4 (\pm 0.4)$, the latter is clearly challenged in α -elements, $[(Na, Mg)/Fe] = -0.1 (\pm 0.2)$. It is difficult to discern whether these stars formed in the bulge and have been flung out or if they have been accreted from the halo (or a dwarf galaxy) and moved inwards. As metal-poor stars in the bulge are thought to be older in absolute age (Tumlinson 2010; Howes et al. 2016; Starkenburg et al. 2017a; El-Badry et al. 2018; Frebel et al. 2019), then these could be extremely valuable objects for studies of the earliest stages of star formation in the Galaxy.

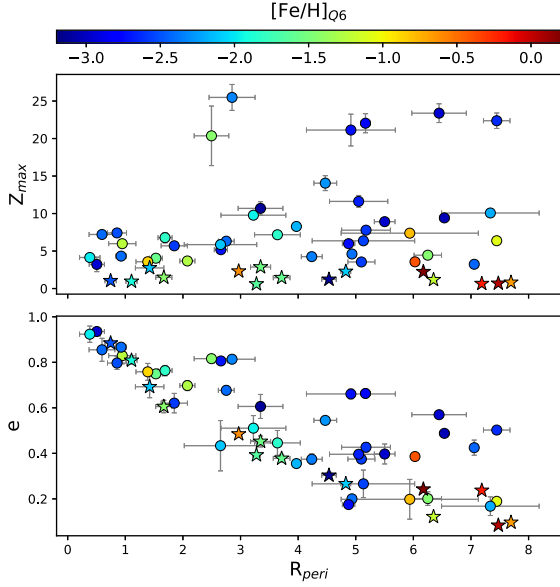


Figure 19. Z_{\max} and eccentricity of the orbits versus pericentric distance R_{peri} for the stars within $R_{\text{apo}} < 30$ kpc. The symbols are the same as in Fig. 18. The very metal poor star confined within $Z_{\max} = 1$ kpc (Pristine_183.6849+04.8619) near $R_{\text{peri}} = 4.5$ kpc can be seen more clearly in this plot than Fig. 18.

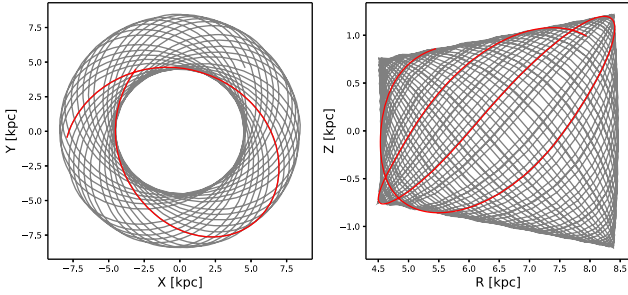


Figure 20. The orbit for the very metal poor star Pristine_183.6849+04.8619, from our adopted Galactic potential. The orbital properties are $R_{\text{apo}} = 8.5$ kpc, $Z_{\max} = 1.2$ kpc, and eccentricity $e=0.3$. A sample single orbit is shown in red.

6.3 Action parameters

The orbital energy (E) and action parameters (vertical J_z , azimuthal J_ϕ) were determined during the Galpy orbit calculations (discussed above); these are shown in Fig. 21 and provided in Table A1. Values are scaled by the solar values, where $J_{\phi\odot} = 2009.92 \text{ km s}^{-1} \text{ kpc}$, $J_{z\odot} = 0.35 \text{ km s}^{-1} \text{ kpc}$, and $E_\odot = -64\,943.61 \text{ (km s}^{-1})^2$. It is worth noting that stars with $J_\phi/J_{\phi\odot} = 1$ rotate like the Sun around the Galactic Centre.

Among the very metal poor stars, we note that they are roughly evenly distributed between retrograde and prograde orbits, i.e. between $-1 < J_\phi/J_{\phi\odot} < 1$. The most retrograde metal-poor star with a bound orbit (near $J_\phi/J_{\phi\odot} = -1$) is Pristine_198.5486+11.4123. This star has $Z_{\max} = 3.2$ kpc, placing it very close to the Galactic plane. Therefore, this star is travelling at nearly the speed of the Sun but in the opposite direction, close to the Galactic plane. This orbit is certainly unusual and suggests that it may have been accreted from a dwarf galaxy; however, its chemistry is like that of a normal metal-poor star, $[\text{Fe}/\text{H}] = -2.5$, $[\text{Mg}/\text{Fe}] = +0.3$, and $[\text{Ba}/\text{Fe}] < +0.4$.

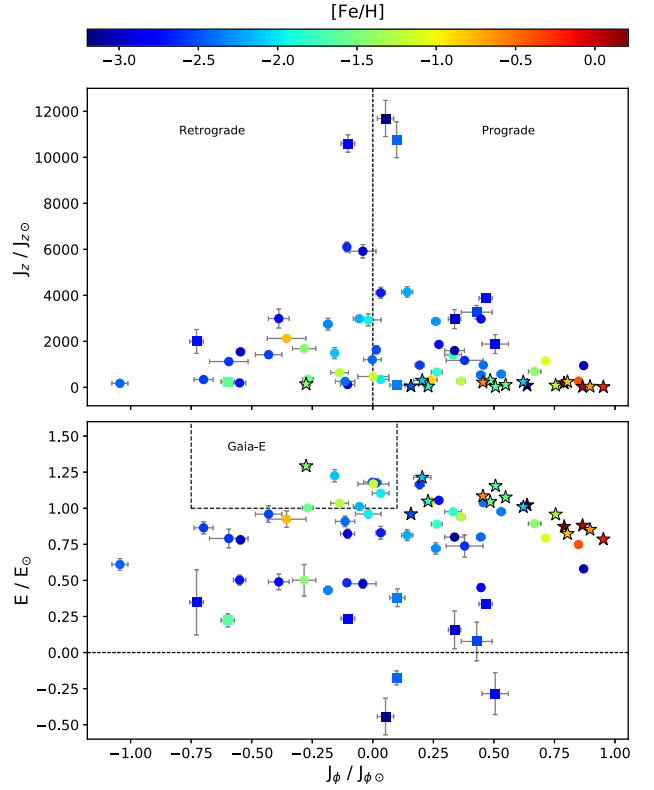


Figure 21. The orbit energies and rotational actions for the 70 high-probability metal-poor stars in this paper. The rotational action J_ϕ ($= L_z$) is compared with the vertical action J_z space (top panel) and the orbit energy (bottom panel), all normalized by the solar values. Prograde and retrograde regions are identified in the top panel. The symbols are as in Fig. 18. The region associated with Gaia-Enceladus is marked, above $E/E_\odot > 1$ and $-0.75 < J_\phi/J_{\phi\odot} < 0.1$ (Belokurov et al. 2018; Haywood et al. 2018; Helmi et al. 2018; Myeong et al. 2018, 2019).

The very metal poor star Pristine_251.4082+12.3657, identified as having the largest R_{apo} value in this sample, is also found to have a large $J_z/J_{z\odot}$ value and an unbound orbit ($E/E_\odot < 0$). In total, the three stars in Fig. 21 appear to have unbound orbits, although we caution that our uncertainties in their orbits are quite small when based on the very small distance errors from the Bayesian inference method. Examination of their parallax errors shows that their orbits could be bound, consistent with $E/E_\odot \sim 0$. In Appendix A, we examine five more stars that appear to be dynamically unbound when their Bayesian inferred distances are used to determine their orbits. Two of those stars were discussed in Section 4.1, and it was shown that the orbital properties for these two metal-rich stars were significantly improved when $1/\text{parallax}$ was adopted for their distances. The same was found for a third star Pristine_213.7879+08.4232, even though this star has been confirmed to be metal poor. The parallax errors for these three stars are all very small, and therefore we have adopted the $1/\text{parallax}$ distance for the orbital analysis of these three stars. Finally, we removed two stars from this kinematic analysis, Pristine_181.4395+01.6294 and Pristine_182.5364+00.9431. Both stars have $R_{\text{apo}} > 500$ kpc and $e \sim 1$, resulting in extreme and unbound orbits for any distance that we adopt.

One of the most exciting discoveries from the *Gaia* DR2 data set has been the identification of the Gaia-Enceladus dwarf galaxy (or galaxies) dissolved into the Milky Way halo. The region where stars may be associated with Gaia-Enceladus is shown in

Fig. 21, i.e. $E/E_{\odot} > 1$ and $-0.75 < J_{\phi}/J_{\phi\odot} < 0.1$ (Belokurov et al. 2018; Haywood et al. 2018; Helmi et al. 2018; Myeong et al. 2018, 2019). This includes eight stars in our sample that range from $-2.5 < [\text{Fe}/\text{H}]_{\text{Q6}} < -1.0$, with a mean metallicity of $<[\text{Fe}/\text{H}] > -2.0 \pm 0.5$; see Table A1. Only one of these stars is sufficiently metal poor to have made it into our detailed analysis sample, *Pristine*_250.6963+08.3743 ($[\text{Fe}/\text{H}] = -2.55 \pm 0.03$). This star has high α -element abundances $[(\text{Ca}, \text{Ti})/\text{Fe}] \sim +0.4$, but lower magnesium such that $[\text{Mg}/(\text{Ca}, \text{Ti})] = -0.3$, which has been seen in some dwarf galaxies (e.g. Tri II, Venn et al. 2017). However, unlike most stars in dwarf galaxies, this star appears to have solar-like $[\text{Ba}/\text{Fe}] \sim 0$ and $[\text{Sc}/\text{Fe}] \sim 0$. It is unclear if this star is a true member of the original Gaia-Enceladus accretion event, but if so it would be among the most metal-poor stars yet found in that system (though also see Monty et al. 2019). As a final test, we examine the action–energy space of the newly discovered Gaia-Sequoia accretion event (Myeong et al. 2018, 2019), i.e. $E/E_{\odot} > 1$ and $J_{\phi}/J_{\phi\odot} < -1.5$, but find no targets in that parameter space.

7 CONCLUSIONS AND FUTURE WORK

The results from our follow-up spectroscopy of 115 bright metal-poor candidates selected from the *Pristine* survey have been presented based on the CFHT ESPaDOnS spectra. We have discovered 28 new very metal poor stars with $[\text{Fe}/\text{H}] < -2.5$ and five stars with $[\text{Fe}/\text{H}] < -3.0$, which imply success rates of 40 (28/70) and 19 per cent (5/27), respectively. These rates are higher than previous surveys, though in line with the *Pristine* medium-resolution programmes. A detailed model atmosphere analysis for the 28 new very metal poor stars has provided stellar parameters and chemical abundances for 10 elements (Na, Mg, Ca, Sc, Ti, Cr, Fe, Ni, Y, and Ba) and Li upper limits. Most stars show chemical abundance patterns that are similar to the normal metal-poor stars in the Galactic halo; however, we also report the discoveries of a new r-process-rich star (*Pristine*_214.5556+07.4670), a new CEMP-s candidate with $[\text{Y}/\text{Ba}] > 0$ (*Pristine*_245.8356+13.8777), and an [Mg/Fe]-challenged star (*Pristine*_251.4082+12.3657), which has an abundance pattern typical of stars in dwarf galaxies or, alternatively, gas enriched by a massive Population III first star exploding as a fall-back supernova. Two stars are also interesting because they are quite Ba poor (*Pristine*_181.4395+01.6294 and *Pristine*_193.8390+11.4150), and resemble stars in the Segue 1 and Hercules UFDs, which have been interpreted as evidence for inhomogeneous enrichment by a single (or few) supernova event, and therefore possibly related to first stars.

The kinematics and orbits for all 70 of the metal-poor candidates have been determined using the *Gaia* DR2 data, our RVs, and adopting the *MWPotential14* in the Galpy package (with a slightly more massive halo). The majority of the confirmed metal-poor stars are members of the Galactic halo, although some stars show unusual kinematics for their chemistry. We report the discovery of a very metal poor ($[\text{Fe}/\text{H}] = -3.2 \pm 0.1$) star (*Pristine*_183.6849+04.8619) with a slightly eccentric ($e = 0.3$) prograde orbit confined to the Galactic plane ($Z_{\text{max}} < 1.2$ kpc). We also find a metal-poor ($[\text{Fe}/\text{H}] = -2.5 \pm 0.1$) star (*Pristine*_198.5486+11.4123) on a highly retrograde orbit ($V = -510 \text{ km s}^{-1}$, $J_{\phi}/J_{\phi\odot} = -1.0$) that remains close to the Galactic plane ($Z_{\text{max}} < 3.2$ kpc). These two stars do not fit standard models for the formation of the Galactic plane, pointing towards more complex origins. An additional eight stars were found to have orbital energy and actions consistent with the Gaia-Enceladus accretion event, including one very metal poor star (*Pristine*_250.6963+08.3743)

with $[\text{Fe}/\text{H}] = -2.5$ and chemical abundances that are common for stars in dwarf galaxies. Finally, eight stars have highly radial orbits that take them deep into the Galactic bulge ($R_{\text{peri}} < 1$ kpc), including two very metal poor stars (*Pristine*_250.6963+08.3743 at $[\text{Fe}/\text{H}] = -2.55 \pm 0.03$, and *Pristine*_201.8710+07.1810 at $[\text{Fe}/\text{H}] = -2.93 \pm 0.11$, the latter star is also low in α -elements). If these stars formed in the bulge, they could be extremely valuable for studies of the earliest conditions for star formation in the Galaxy.

Currently, we are running a Gemini/GRACES Large and Long Program to follow up with high-SNR (> 100) spectra for our best metal-poor candidates ($[\text{Fe}/\text{H}] < -3.5$) and with $V < 17$ selected from medium-resolution spectroscopy. We also plan to observe a selection of these stars with the upcoming Gemini GHOST spectrograph (Chene et al. 2014; Sheinis et al. 2017), which is anticipated to have excellent throughput at blue-UV wavelengths, providing far more iron-group lines for stellar parameter assessments and many more spectral lines of heavy neutron-capture (and light) elements.

In the near future, massively multiplexed high-resolution spectroscopic surveys ($R > 20\,000$) will be initiated, including the European WEAVE survey at the INTs (Dalton et al. 2012), the 4MOST survey at ESO (De Jong et al. 2019), and the SDSS-V survey comprising fields in both the Northern and Southern hemispheres (Kollmeier et al. 2017). These will provide the truly large statistical samples needed for the studies of the metal-poor Galaxy.

ACKNOWLEDGEMENTS

This work is based on observations obtained at the CFHT that is operated by the National Research Council of Canada, the Institut National des Sciences de l’Univers of the Centre National de la Recherche Scientifique of France, and the University of Hawaii. This work has made use of data from the European Space Agency (ESA) mission *Gaia* (<https://www.cosmos.esa.int/gaia>), processed by the *Gaia* Data Processing and Analysis Consortium (DPAC; <https://www.cosmos.esa.int/web/gaia/dpac/consortium>). Funding for the DPAC has been provided by national institutions, in particular the institutions participating in the *Gaia* Multilateral Agreement. This research has made use of the SIMBAD data base, operated at CDS, Strasbourg, France (Wenger et al. 2000).

The authors wish to thank David Yong and Ian Roederer for helpful discussions on the detailed abundances of the new metal-poor stars. We are also grateful to the anonymous referee for their comments and support.

This work was funded in part through the National Science and Engineering Research Council Discovery Grants programme and the CREATE training programme on New Technologies for Canadian Observatories. The authors thank the International Space Science Institute (ISSI) in Berne, Switzerland, for providing financial support and meeting facilities to the international team *Pristine*. FS and NFM gratefully acknowledge funding from CNRS/INSU through the Programme National Galaxies et Cosmologie and through the CNRS grant PICS07708. FS thanks the Initiative d’Excellence IdEx from the University of Strasbourg and the Programme Doctoral International PDI for funding his PhD. This work has been published under the framework of the IdEx Unistra and benefits from funding from the state managed by the French National Research Agency (ANR) as part of the investments for the future program. JIGH acknowledges financial support from the Spanish Ministry of Science, Innovation and Universities (MICIU) under

the 2013 Ramón y Cajal program MICIU RYC-2013-14875, and also from the Spanish ministry project MICIU AYA2017-86389-P.

The authors wish to recognize and acknowledge the very significant cultural role and reverence that the summit of Maunakea has always had within the indigenous Hawaiian community. We are most fortunate to have had the opportunity to conduct observations from this mountain.

REFERENCES

- Abadi M. G., Navarro J. F., Fardal M., Babul A., Steinmetz M., 2010, *MNRAS*, 407, 435
- Abel T., Bryan G. L., Norman M. L., 2002, *Science*, 295, 93
- Aguado D. et al., 2019a, *MNRAS*, 490, 2241
- Aguado D. S., González Hernández J. I., Allende Prieto C., Rebolo R., 2019b, *ApJ*, 874, L21
- Allende Prieto C., Beers T. C., Wilhelm R., Newberg H. J., Rockosi C. M., Yanny B., Lee Y. S., 2006, *ApJ*, 636, 804
- Amarsi A. M., Lind K., Asplund M., Barklem P. S., Collet R., 2016, *MNRAS*, 463, 1518
- Aoki W., Norris J. E., Ryan S. G., Beers T. C., Ando H., 2002, *ApJ*, 576, L141
- Arentsen A., Starkenburg E., Shetrone M. D., Venn K. A., Depagne É., McConnachie A. W., 2019, *A&A*, 621, A108
- Asplund M., Grevesse N., Sauval A. J., Scott P., 2009, *ARA&A*, 47, 481
- Bailer-Jones C. A. L., Rybizki J., Fouesneau M., Mantelet G., Andrae R., 2018, *AJ*, 156, 58
- Barbá R. H., Minniti D., Geisler D., Alonso-García J., Hempel M., Monachesi A., Arias J. I., Gómez F. A., 2019, *ApJ*, 870, L24
- Beers T. C., Christlieb N., 2005, *ARA&A*, 43, 531
- Beers T. C., Preston G. W., Shectman S. A., 1992, *AJ*, 103, 1987
- Belokurov V., Erkal D., Evans N. W., Koposov S. E., Deason A. J., 2018, *MNRAS*, 478, 611
- Bergemann M., Cescutti G., 2010, *A&A*, 522, A9
- Bird S. A., Xue X.-X., Liu C., Shen J., Flynn C., Yang C., 2019, *AJ*, 157, 104
- Blackwell D. E., Petford A. D., Shallis M. J., 1979, *MNRAS*, 186, 657
- Bland-Hawthorn J., Gerhard O., 2016, *ARA&A*, 54, 529
- Bonifacio P. et al., 2018, *A&A*, 612, A65
- Bonifacio P. et al., 2019, *MNRAS*, 487, 3797
- Bovy J., 2015, *ApJS*, 216, 29
- Bromm V., 2013, *Rep. Prog. Phys.*, 76, 112901
- Caffau E. et al., 2012, *A&A*, 542, A51
- Caffau E. et al., 2017, *Astron. Nachr.*, 338, 686
- Caffau E. et al., 2019, *A&A*, 628, A46
- Casagrande L. et al., 2016, *MNRAS*, 455, 987
- Chene A.-N. et al., 2014, in Ramón N., Colin R. C., Allison A. B., eds, Proc. SPIE Conf. Ser. Vol. 9151, Advances in Optical and Mechanical Technologies for Telescopes and Instrumentation. SPIE, Bellingham, p. 915147
- Choi J., Dotter A., Conroy C., Cantiello M., Paxton B., Johnson B. D., 2016, *ApJ*, 823, 102
- Christlieb N. et al., 2002, *Nature*, 419, 904
- Christlieb N. et al., 2004, *A&A*, 428, 1027
- Christlieb N., Schörck T., Frebel A., Beers T. C., Wisotzki L., Reimers D., 2008, *A&A*, 484, 721
- Clark P. C., Glover S. C. O., Smith R. J., Greif T. H., Klessen R. S., Bromm V., 2011, *Science*, 331, 1040
- Cohen J. G., Kirby E. N., 2012, *ApJ*, 760, 86
- Collet R., Nordlund Å., Asplund M., Hayek W., Trampedach R., 2018, *MNRAS*, 475, 3369
- Cui X.-Q. et al., 2012, *Res. Astron. Astrophys.*, 12, 1197
- Curtis S., Ebinger K., Fröhlich C., Hempel M., Perego A., Liebendörfer M., Thielemann F.-K., 2019, *ApJ*, 870, 2
- DaCosta G. S. et al., 2019, *MNRAS*, 489, 5900
- Dalton G. et al., 2012, in Ian S. M., Suzanne K. R., Hideki T., eds, Proc. SPIE Conf. Ser. Vol. 8446, Ground-based and Airborne Instrumentation for Astronomy IV. SPIE, Bellingham, p. 84460P
- Dawson K. S. et al., 2013, *AJ*, 145, 10
- De Jong R. S., Others A., Others B., 4MOST team, 2019, *The Messenger*, 175, 3
- Depagne E. et al., 2002, *A&A*, 390, 187
- Donati J. F., Semel M., Carter B. D., Rees D. E., Collier Cameron A., 1997, *MNRAS*, 291, 658
- Donati J. F., Catala C., Landstreet J. D., Petit P., 2006, in Casini R., Lites B. W., eds, ASP Conf. Ser. Vol. 358, Solar Polarization 4. Astron. Soc. Pac., San Francisco, p. 362
- Dotter A., 2016, *ApJS*, 222, 8
- Eisenstein D. J. et al., 2011, *AJ*, 142, 72
- El-Badry K. et al., 2018, *MNRAS*, 480, 652
- Frebel A., Norris J. E., 2015, *ARA&A*, 53, 631
- Frebel A. et al., 2006, *ApJ*, 652, 1585
- Frebel A., Simon J. D., Kirby E. N., 2014, *ApJ*, 786, 74
- Frebel A., Ji A. P., Ezzeddine R., Hansen T. T., Chiti A., Thompson I. B., Merle T., 2019, *ApJ*, 871, 146
- Freeman K., Bland-Hawthorn J., 2002, *ARA&A*, 40, 487
- Gaia Collaboration, Brown A. G. A., Vallenari A., Prusti T., de Bruijne J. H. J., Babusiaux C., Bailer-Jones C. A. L., 2018, *A&A*, 616, A1
- Gianninas A., Curd B., Thorstensen J. R., Kilic M., Bergeron P., Andrews J. J., Canton P., Agüeros M. A., 2015, *MNRAS*, 449, 3966
- González Hernández J. I., Bonifacio P., 2009, *A&A*, 497, 497
- Greif T. H., 2015, *Comput. Astrophys. Cosmol.*, 2, 3
- Gustafsson B., Edvardsson B., Eriksson K., Jørgensen U. G., Nordlund Å., Plez B., 2008, *A&A*, 486, 951
- Hartwig T. et al., 2018, *MNRAS*, 478, 1795
- Hattori K., Erkal D., Sanders J. L., 2016, *MNRAS*, 460, 497
- Hayes C. R. et al., 2018, *ApJ*, 852, 49
- Haywood M., Di Matteo P., Lehnert M. D., Snaith O., Khoperskov S., Gómez A., 2018, *ApJ*, 863, 113
- Heger A., Woosley S. E., 2010, *ApJ*, 724, 341
- Helmi A., White S. D. M., de Zeeuw P. T., Zhao H., 1999, *Nature*, 402, 53
- Helmi A., Babusiaux C., Koppelman H. H., Massari D., Veljanoski J., Brown A. G. A., 2018, *Nature*, 563, 85
- Henden A. A., 2019, J. Am. Assoc. Var. Star Obs. (JAAVSO), 47, 130
- Hernitschek N. et al., 2016, *ApJ*, 817, 73
- Hill V., Christlieb N., Beers T. C., Barklem P. S., Kratz K.-L., Nordström B., Pfeiffer B., Farouqi K., 2017, *A&A*, 607, A91
- Hirano S., Hosokawa T., Yoshida N., Omukai K., Yorke H. W., 2015, *MNRAS*, 448, 568
- Howes L. M. et al., 2016, *MNRAS*, 460, 884
- Ibata R. A., Gilmore G., Irwin M. J., 1994, *Nature*, 370, 194
- Ibata R., Chapman S., Ferguson A. M. N., Irwin M., Lewis G., McConnachie A., 2004, *MNRAS*, 351, 117
- Ishigaki M. N., Tominaga N., Kobayashi C., Nomoto K., 2018, *ApJ*, 857, 46
- Ivezić Ž. et al., 2008, *ApJ*, 684, 287
- Jablunka P. et al., 2015, *A&A*, 583, A67
- Ji A. P., Frebel A., Simon J. D., Chiti A., 2016, *ApJ*, 830, 93
- Ji A. P., Drouot M. R., Hansen T. T., 2019, *ApJ*, 882, 170
- Jones S., Côté B., Roepke F. K., Wanajo S., 2019, *ApJ*, 882, 170
- Jordi K., Grebel E. K., Ammon K., 2006, *A&A*, 460, 339
- Keller S. C. et al., 2007, *PASA*, 24, 1
- Keller S. C. et al., 2014, *Nature*, 506, 463
- Kielty C. L., Venn K. A., Loewen N. B., Shetrone M. D., Placco V. M., Jahandar F., Mészáros S., Martell S. L., 2017, *MNRAS*, 471, 404
- Koch A., Feltzing S., Adén D., Matteucci F., 2013, *A&A*, 554, A5
- Koesterke L., Allende Prieto C., Lambert D. L., 2008, *ApJ*, 680, 764
- Kollmeier J. A. et al., 2017, preprint (arXiv:1711.03234)
- Kurucz R. L., 2005, Mem. Soc. Astron. Ital. Suppl., 8, 14
- Lamb M. et al., 2017, *MNRAS*, 465, 3536
- Lind K., Bergemann M., Asplund M., 2012, *MNRAS*, 427, 50
- Lindgren L. et al., 2018, *A&A*, 616, A2
- Lokhorst D. et al., 2016, *ApJ*, 819, 124

- Longeard N. et al., 2018, *MNRAS*, 480, 2609
- Longeard N. et al., 2019, *MNRAS*, 491, 356
- McWilliam A., Wallerstein G., Mottini M., 2013, *ApJ*, 778, 149
- Mardini M. K. et al., 2019, *ApJ*, 875, 89
- Mashonkina L., Jablonka P., Pakhomov Y., Sitnova T., North P., 2017a, *A&A*, 604, A129
- Mashonkina L., Sitnova T., Belyaev A. K., 2017b, *A&A*, 605, A53
- Mashonkina L., Jablonka P., Sitnova T., Pakhomov Y., North P., 2017c, *A&A*, 608, A89
- Mashonkina L., Sitnova T., Yakovleva S. A., Belyaev A. K., 2019, *A&A*, 631, 43
- Monty S., Venn K. A., Lane J. M. M., Lokhorst D., Yong D., 2019, preprint (arXiv:1909.11969)
- Müller B. et al., 2019, *MNRAS*, 484, 3307
- Myeong G. C., Evans N. W., Belokurov V., Sanders J. L., Koposov S. E., 2018, *ApJ*, 863, L28
- Myeong G. C., Vasiliev E., Iorio G., Evans N. W., Belokurov V., 2019, *MNRAS*, 488, 1235
- Nakamura F., Umemura M., 2001, *ApJ*, 548, 19
- Navarro J. F., Frenk C. S., White S. D. M., 1997, *ApJ*, 490, 493
- Nissen P. E., Schuster W. J., 2010, *A&A*, 511, L10
- Nordlander T. et al., 2019, *MNRAS*, 488, L109
- Norris J. E. et al., 2013, *ApJ*, 762, 28
- Norris J. E., Yong D., Venn K. A., Gilmore G., Casagrande L., Dotter A., 2017, *ApJS*, 230, 28
- O'Brian T. R., Wickliffe M. E., Lawler J. E., Whaling W., Brault J. W., 1991, *J. Opt. Soc. Am. B Opt. Phys.*, 8, 1185
- Paxton B., Bildsten L., Dotter A., Herwig F., Lesaffre P., Timmes F., 2011, *ApJS*, 192, 3
- Pearson S., Price-Whelan A. M., Johnston K. V., 2017, *Nat. Astron.*, 1, 633
- Price-Whelan A. M., Sesar B., Johnston K. V., Rix H.-W., 2016, *ApJ*, 824, 104
- Raassen A. J. J., Uylings P. H. M., 1998, *A&A*, 340, 300
- Robin A. C., Reylé C., Derrière S., Picaud S., 2003, *A&A*, 409, 523
- Roederer I. U., 2011, *ApJ*, 732, L17
- Roederer I. U., Cowan J. J., Karakas A. I., Kratz K.-L., Lugaro M., Simmerer J., Farouqi K., Sneden C., 2010, *ApJ*, 724, 975
- Roederer I. U., Preston G. W., Thompson I. B., Shectman S. A., Sneden C., Burley G. S., Kelson D. D., 2014, *AJ*, 147, 136
- Roederer I. U., Hattori K., Valluri M., 2018a, *AJ*, 156, 179
- Roederer I. U., Sneden C., Lawler J. E., Sobeck J. S., Cowan J. J., Boesgaard A. M., 2018b, *ApJ*, 860, 125
- Sakari C. M. et al., 2018a, *ApJ*, 854, L20
- Sakari C. M. et al., 2018b, *ApJ*, 868, 110
- Salvadori S., Bonifacio P., Caffau E., Korotin S., Andreevsky S., Spite M., Skúladóttir Á., 2019, *MNRAS*, 487, 4261
- Schlaufman K. C., Casey A. R., 2014, *ApJ*, 797, 13
- Schlegel D. J., Finkbeiner D. P., Davis M., 1998, *ApJ*, 500, 525
- Schneider R., Ferrara A., Salvaterra R., Omukai K., Bromm V., 2003, *Nature*, 422, 869
- Schönrich R., Binney J., Dehnen W., 2010, *MNRAS*, 403, 1829
- Schörck T. et al., 2009, *A&A*, 507, 817
- Sestito F. et al., 2019, *MNRAS*, 484, 2166
- Sheinis A. I. et al., 2017, in Christopher J. E., Luc S., Hideki T., eds, Proc. SPIE Conf. Ser. Vol. 9908, Ground-based and Airborne Instrumentation for Astronomy VI. SPIE, Bellingham, p. 990817
- Simon J. D., 2018, *ApJ*, 863, 89
- Sitnova T. et al., 2015, *ApJ*, 808, 148
- Sitnova T. M., Mashonkina L. I., Ryabchikova T. A., 2016, *MNRAS*, 461, 1000
- Sneden C. A., 1973, PhD thesis, Univ. Texas at Austin
- Sobeck J. S. et al., 2011, *AJ*, 141, 175
- Spergel D. N. et al., 2003, *ApJS*, 148, 175
- Starkenburg E., Shetrone M. D., McConnachie A. W., Venn K. A., 2014, *MNRAS*, 441, 1217
- Starkenburg E., Oman K. A., Navarro J. F., Crain R. A., Fattahi A., Frenk C. S., Sawala T., Schaye J., 2017a, *MNRAS*, 465, 2212
- Starkenburg E. et al., 2017b, *MNRAS*, 471, 2587
- Starkenburg E. et al., 2018, *MNRAS*, 481, 3838
- Stetson P. B., Pancino E., 2008, *PASP*, 120, 1332
- Suda T. et al., 2017, *PASJ*, 69, 76
- Thielemann F.-K., Isern J., Perego A., von Ballmoos P., 2018, *Space Sci. Rev.*, 214, 62
- Tolstoy E., Hill V., Tosi M., 2009, *ARA&A*, 47, 371
- Tumlinson J., 2010, *ApJ*, 708, 1398
- Venn K. A., Irwin M., Shetrone M. D., Tout C. A., Hill V., Tolstoy E., 2004, *AJ*, 128, 1177
- Venn K. A. et al., 2012, *ApJ*, 751, 102
- Venn K. A., Starkenburg E., Malo L., Martin N., Laevens B. P. M., 2017, *MNRAS*, 466, 3741
- Wanajo S., 2018, *ApJ*, 868, 65
- Wenger M. et al., 2000, *A&AS*, 143, 9
- Woosley S. E., Heger A., Weaver T. A., 2002, *Rev. Mod. Phys.*, 74, 1015
- Yanny B. et al., 2009, *AJ*, 137, 4377
- Yong D. et al., 2013, *ApJ*, 762, 26
- York D. G. et al., 2000, *AJ*, 120, 1579
- Youakim K. et al., 2017, *MNRAS*, 472, 2963
- Zinn J. C., Pinsonneault M. H., Huber D., Stello D., 2019, *ApJ*, 878, 136

SUPPORTING INFORMATION

Supplementary data are available at *MNRAS* online.

Table 1. Metal-poor targets (115) from the original *Pristine* survey footprint.

Table 2. *Gaia* DR2 parallaxes, and the derived distances (D), temperatures (T), and surface gravities ($\log g$) from the Bayesian inference method (see Section 4.1, assuming $[\text{Fe}/\text{H}]_p$).

Table 3. Line list from Norris et al. (2017) with atomic data updates from *linemake* (see the text).

Please note: Oxford University Press is not responsible for the content or functionality of any supporting materials supplied by the authors. Any queries (other than missing material) should be directed to the corresponding author for the article.

APPENDIX A

The UVW velocities for the 70 highly probable metal-poor stars in this sample are given in Table A1.

Five stars were identified for a more careful dynamical analysis in Section 6.1. When their distances were determined from the Bayesian inference method, these stars had highly energetic and unbound orbits ($E/E_\odot < -0.5$), with $R_{\text{apo}} > 500$ kpc. These five stars are shown in Fig. A1.

As two of these stars (Pristine_200.5298+08.9768 and Pristine_187.9785+08.7294) were found to have higher metallicities than had been adopted for the MIST stellar isochrone in the Bayesian inference method, then we assumed that their Bayesian inferred distances were unreliable. Adopting their distances as $1/\text{parallax}$ from the *Gaia* DR2 data base, then we found sensible orbits and dynamical parameters for both the stars. Furthermore, the parallax errors were small for both the stars.

We found that the orbit solution for a third star (Pristine_213.7879+08.4232) was also significantly improved by rejecting the Bayesian inferred distance in favour of the $1/\text{parallax}$ value. Again, the parallax error is small, and the resulting orbital properties are less peculiar. It is not clear why the Bayesian method did not work for this star; however, we note that this was a target that we observed very early on and it is no longer in the *Pristine* survey catalogue. Investigating this star a bit further, we notice that the $1/\text{parallax}$ distance is closer than the Bayesian inferred distance, suggesting that the surface gravity for this star may be slightly

Table A1. Orbit and Action parameters for the 70 metal-poor candidates from the *Pristine* survey.

RA (deg)	DEC (deg)	pmra ($\mu\text{as yr}^{-1}$)	pmdec ($\mu\text{as yr}^{-1}$)	U (km s^{-1})	V (km s^{-1})	W (km s^{-1})	R_{apo} (kpc)	R_{peri} (kpc)	Eccentricity	Z_{max} (kpc)	$J_{\phi}/J_{\phi\odot}$	$J_z/J_{z\odot}$	E/E_{\odot}
180.2206	09.5683	1.47 \pm 0.08	-3.68 \pm 0.06	175.69 \pm 6.90	-143.29 \pm 5.31	-26.54 \pm 1.96	23.5 \pm 1.3	6.6 \pm 0.5	0.57 \pm 0.01	23.4 \pm 1.3	-0.04 \pm 0.05	5918.45 \pm 289.73	0.477 \pm -0.032
180.3789	00.9470	-14.76 \pm 0.92	-5.28 \pm 0.49	-101.97 \pm 6.13	-73.77 \pm 5.78	-100.36 \pm 2.89	9.4 \pm 0.3	6.3 \pm 0.2	0.20 \pm 0.03	4.5 \pm 0.4	0.67 \pm 0.03	689.95 \pm 82.44	0.893 \pm -0.011
181.2243	07.4160	1.98 \pm 0.08	-8.19 \pm 0.05	60.40 \pm 1.88	-4.87 \pm 1.86	-161.93 \pm 0.92	19.0 \pm 0.1	6.5 \pm 0.1	0.49 \pm 0.01	9.4 \pm 0.1	0.87 \pm 0.01	948.17 \pm 13.67	0.58 \pm -0.003
181.3464	11.6698	-14.31 \pm 0.06	2.84 \pm 0.03	-39.73 \pm 0.65	-15.73 \pm 0.26	6.31 \pm 0.48	8.8 \pm 0.0	7.5 \pm 0.1	0.08 \pm 0.00	0.7 \pm 0.1	0.87 \pm 0.0	32.49 \pm 0.77	0.881 \pm -0.001
181.3699	11.7636	-9.20 \pm 0.06	-4.69 \pm 0.03	-66.05 \pm 3.11	-116.49 \pm 4.39	44.36 \pm 1.64	8.9 \pm 0.1	3.4 \pm 0.2	0.45 \pm 0.02	2.9 \pm 0.1	0.48 \pm 0.02	303.79 \pm 5.57	1.045 \pm -0.002
181.4395	01.6294	-3.34 \pm 0.08	-9.14 \pm 0.04	134.17 \pm 3.39	-768.5 \pm 11.62	-177.4 \pm 6.21	2345.5 \pm 124.2	18.1 \pm 0.3	0.98 \pm 0.00	1049.8 \pm 44.4	-2.4 \pm 0.05	16291.42 \pm 799.81	-1.919 \pm -0.125
181.6953	13.8075	-16.18 \pm 0.06	-3.44 \pm 0.03	164.22 \pm 6.23	-156.8 \pm 5.18	28.91 \pm 1.87	11.7 \pm 0.3	2.1 \pm 0.1	0.70 \pm 0.02	3.7 \pm 0.2	0.36 \pm 0.02	271.81 \pm 17.54	0.94 \pm -0.012
182.5364	00.9431	-43.19 \pm 0.08	-49.25 \pm 0.06	-124.30 \pm 7.39	-702.83 \pm 30.92	-103.95 \pm 15.46	541.2 \pm 437.2	7.9 \pm 0.3	0.94 \pm 0.04	164.9 \pm 134.9	-1.77 \pm 0.12	766.27 \pm 167.98	-0.66 \pm -0.285
183.6849	04.8619	-0.70 \pm 0.11	-12.87 \pm 0.12	31.50 \pm 1.67	-68.32 \pm 2.46	11.5 \pm 1.24	8.5 \pm 0.1	4.5 \pm 0.1	0.30 \pm 0.01	1.2 \pm 0.1	0.64 \pm 0.01	84.71 \pm 4.01	1.022 \pm -0.005
185.4110	07.4777	-70.21 \pm 0.07	-37.42 \pm 0.04	-146.72 \pm 3.89	-305.15 \pm 5.95	85.86 \pm 1.97	10.7 \pm 0.2	1.5 \pm 0.1	0.75 \pm 0.01	4.0 \pm 0.2	-0.27 \pm 0.02	352.7 \pm 24.77	1.002 \pm -0.012
187.9785	08.7294	-20.24 \pm 0.10	2.84 \pm 0.05	121.345 \pm 6.39	-32.49 \pm 2.74	-55.94 \pm 0.52	11.5 \pm 0.2	6.0 \pm 0.1	0.32 \pm 0.02	2.9 \pm 0.2	0.80 \pm 0.01	240.41 \pm 19.72	0.823 \pm 0.004
188.1264	08.7740	-6.31 \pm 0.08	-7.70 \pm 0.05	-47.33 \pm 2.51	-247.10 \pm 14.74	-126.96 \pm 4.56	9.9 \pm 0.2	3.2 \pm 0.6	0.51 \pm 0.06	9.8 \pm 0.2	-0.02 \pm 0.05	2933.74 \pm 261.61	0.96 \pm -0.028
189.9449	11.5534	3.40 \pm 0.06	-55.97 \pm 0.05	257.42 \pm 4.44	-358.77 \pm 6.12	-88.47 \pm 2.14	24.8 \pm 1.4	2.7 \pm 0.1	0.81 \pm 0.00	5.2 \pm 0.4	-0.55 \pm 0.03	194.46 \pm 6.74	0.502 \pm -0.034
190.6313	08.5137	-13.53 \pm 0.10	-19.24 \pm 0.05	-34.76 \pm 1.66	-330.56 \pm 21.07	-163.11 \pm 6.21	8.7 \pm 0.4	5.9 \pm 1.2	0.20 \pm 0.09	7.4 \pm 0.3	-0.36 \pm 0.08	2128.14 \pm 48.96	0.924 \pm -0.057
193.1159	08.0557	6.70 \pm 0.06	-57.85 \pm 0.04	140.26 \pm 3.27	-169.78 \pm 3.91	-30.26 \pm 1.81	10.5 \pm 0.1	1.1 \pm 0.1	0.81 \pm 0.02	1.0 \pm 0.1	0.23 \pm 0.02	44.76 \pm 2.42	1.048 \pm -0.005
193.5533	11.5037	1.37 \pm 0.05	-1.21 \pm 0.03	7.22 \pm 0.13	-4.11 \pm 0.12	14.51 \pm 0.48	9.3 \pm 0.0	7.7 \pm 0.0	0.10 \pm 0.00	0.8 \pm 0.1	0.9 \pm 0.0	40.68 \pm 1.03	0.852 \pm -0.0
193.8390	11.4150	0.98 \pm 0.07	-2.19 \pm 0.04	178.73 \pm 4.59	-112.05 \pm 3.29	-51.18 \pm 1.35	33.6 \pm 2.0	13.8 \pm 0.5	0.42 \pm 0.01	33.5 \pm 1.9	-0.1 \pm 0.03	10599.81 \pm 378.3	0.235 \pm -0.029
196.3755	08.5138	-1.46 \pm 0.08	-6.48 \pm 0.06	106.90 \pm 4.63	-317.24 \pm 12.03	-179.96 \pm 4.05	23.9 \pm 2.2	4.9 \pm 0.8	0.66 \pm 0.02	21.1 \pm 2.1	-0.39 \pm 0.04	2991.74 \pm 412.01	0.49 \pm -0.054
196.4117	14.3176	-18.78 \pm 0.06	-9.71 \pm 0.04	-35.04 \pm 0.48	-40.59 \pm 0.87	-51.6 \pm 0.49	8.1 \pm 0.1	6.4 \pm 0.2	0.12 \pm 0.00	1.2 \pm 0.1	0.75 \pm 0.0	86.87 \pm 1.97	0.958 \pm -0.002
196.5453	12.1211	25.63 \pm 0.07	-56.26 \pm 0.04	321.48 \pm 11.69	-196.02 \pm 6.99	-44.4 \pm 3.69	31.8 \pm 3.5	0.5 \pm 0.1	0.97 \pm 0.01	4.0 \pm 0.7	0.1 \pm 0.03	96.63 \pm 5.86	0.38 \pm -0.061
198.5486	11.4123	-47.39 \pm 0.06	-46.31 \pm 0.04	-86.24 \pm 1.88	-510.48 \pm 8.99	8.85 \pm 1.27	17.6 \pm 1.6	7.1 \pm 0.1	0.42 \pm 0.03	3.2 \pm 0.4	-1.04 \pm 0.03	174.96 \pm 8.22	0.61 \pm -0.041
200.0999	13.7228	-4.09 \pm 0.06	-1.02 \pm 0.04	-223.20 \pm 6.01	-340.64 \pm 7.01	206.07 \pm 0.83	90.2 \pm 10.1	9.9 \pm 0.7	0.80 \pm 0.01	89.2 \pm 9.5	0.10 \pm 0.01	10765.9 \pm 780.77	-0.176 \pm -0.048
200.5298	08.9768	-20.91 \pm 0.08	-12.61 \pm 0.04	-69.46 \pm 8.35	-233.94 \pm 18.62	78.19 \pm 1.31	12.9 \pm 51.3	0.4 \pm 0.2	0.92 \pm 0.06	5.8 \pm 19.7	0.00 \pm 0.06	472.31 \pm 14.80	1.17 \pm 0.01
200.7620	09.4375	8.03 \pm 0.06	-4.98 \pm 0.03	93.28 \pm 1.30	1.62 \pm 0.24	8.97 \pm 0.59	13.6 \pm 0.1	6.0 \pm 0.1	0.39 \pm 0.00	3.6 \pm 0.1	0.85 \pm 0.0	273.96 \pm 7.04	0.748 \pm -0.003
201.1158	15.4381	-8.64 \pm 0.06	-1.74 \pm 0.05	-62.21 \pm 1.65	-67.21 \pm 1.82	2.9 \pm 0.53	8.3 \pm 0.0	4.8 \pm 0.1	0.27 \pm 0.01	2.3 \pm 0.1	0.62 \pm 0.01	240.53 \pm 10.05	1.01 \pm -0.002
201.3732	08.4513	-17.04 \pm 0.07	-3.15 \pm 0.04	-144.52 \pm 6.99	-175.08 \pm 7.42	56.68 \pm 0.87	10.1 \pm 0.3	1.4 \pm 0.2	0.76 \pm 0.04	3.6 \pm 0.2	0.24 \pm 0.03	321.08 \pm 11.49	1.049 \pm -0.012
201.8711	07.1810	-78.20 \pm 0.08	-13.09 \pm 0.05	-239.77 \pm 7.57	-265.05 \pm 7.84	58.94 \pm 1.00	15.0 \pm 0.8	5.5 \pm 0.1	0.94 \pm 0.01	3.2 \pm 1.0	-0.1 \pm 0.03	124.81 \pm 1.95	0.822 \pm -0.032
202.3435	13.2291	-4.59 \pm 0.05	-26.08 \pm 0.02	145.13 \pm 4.50	-264.49 \pm 9.62	36.58 \pm 2.37	10.1 \pm 0.2	1.0 \pm 0.2	0.83 \pm 0.04	6.0 \pm 0.2	-0.14 \pm 0.04	640.0 \pm 15.69	1.035 \pm -0.016
203.2831	13.6326	-0.91 \pm 0.05	-5.35 \pm 0.03	105.34 \pm 3.35	-284.55 \pm 6.72	-203.82 \pm 1.65	27.6 \pm 1.3	2.9 \pm 0.4	0.81 \pm 0.02	25.5 \pm 1.7	-0.19 \pm 0.02	2748.57 \pm 254.75	0.432 \pm -0.028
204.9008	10.5513	10.65 \pm 0.06	-33.88 \pm 0.05	103.14 \pm 8.51	-106.04 \pm 6.33	-310.79 \pm 3.75	31.5 \pm 1.5	6.2 \pm 0.2	0.67 \pm 0.02	28.3 \pm 1.6	0.47 \pm 0.03	3873.18 \pm 104.35	0.336 \pm -0.022
205.1342	13.8234	-8.1 \pm 0.07	-2.72 \pm 0.06	-46.57 \pm 5.60	-136.76 \pm 8.5	137.12 \pm 1.18	9.5 \pm 0.3	3.6 \pm 0.4	0.45 \pm 0.05	7.2 \pm 0.4	0.33 \pm 0.03	1413.11 \pm 31.15	0.976 \pm -0.003
205.8131	15.3832	10.45 \pm 0.06	-30.98 \pm 0.04	190.87 \pm 5.92	-113.35 \pm 4.09	64.18 \pm 2.01	14.3 \pm 0.3	2.8 \pm 0.1	0.68 \pm 0.02	6.3 \pm 0.3	0.45 \pm 0.02	541.15 \pm 12.38	0.801 \pm -0.001
206.3487	09.3099	1.22 \pm 0.06	-67.65 \pm 0.04	324.56 \pm 5.30	-385.14 \pm 7.22	-2.39 \pm 3.00	41.4 \pm 3.5	2.7 \pm 0.1	0.88 \pm 0.01	10.2 \pm 0.8	-0.6 \pm 0.03	246.21 \pm 2.21	0.223 \pm -0.045
208.0798	04.4266	2.02 \pm 0.07	-12.87 \pm 0.07	81.27 \pm 8.37	-120.10 \pm 8.76	-205.75 \pm 5.62	13.8 \pm 0.7	3.4 \pm 0.4	0.61 \pm 0.05	10.7 \pm 0.9	0.34 \pm 0.04	1600.13 \pm 53.45	0.8 \pm -0.02
209.9364	15.9251	1.78 \pm 0.08	-13.73 \pm 0.07	56.47 \pm 3.89	-87.63 \pm 3.89	-116.8 \pm 1.42	9.3 \pm 0.1	4.2 \pm 0.2	0.37 \pm 0.02	4.3 \pm 0.1	0.53 \pm 0.02	578.82 \pm 17.2	0.976 \pm -0.002
210.0166	14.6289	-9.65 \pm 0.05	-10.23 \pm 0.05	-0.72 \pm 1.52	-377.07 \pm 19.55	76.2 \pm 0.60	8.8 \pm 0.5	5.1 \pm 0.9	0.27 \pm 0.06	6.4 \pm 0.4	-0.43 \pm 0.05	1421.89 \pm 143.6	0.959 \pm -0.057
210.8632	08.1797	-5.11 \pm 0.06	-13.39 \pm 0.05	41.58 \pm 2.50	-170.72 \pm 9.11	-49.28 \pm 2.09	7.8 \pm 0.1	1.4 \pm 0.3	0.69 \pm 0.05	2.8 \pm 0.1	0.20 \pm 0.04	300.71 \pm 22.72	1.214 \pm -0.004
213.2814	14.8983	-0.27 \pm 0.08	-13.33 \pm 0.07	74.25 \pm 1.18	-105.65 \pm 1.51	-42.69 \pm 0.64	8.6 \pm 0.1	3.0 \pm 0.1	0.48 \pm 0.01	2.3 \pm 0.1	0.45 \pm 0.01	220.76 \pm 4.28	1.084 \pm -0.002
213.7879	08.4232	5.67 \pm 0.07	-15.94 \pm 0.07	-114.70 \pm 18.31	-194.86 \pm 15.19	194.86 \pm 15.19	15.8 \pm 2.8	3.0 \pm 0.7	0.67 \pm 0.11	10.8 \pm 2.4	0.38 \pm 0.08	1174.7 \pm 64.97	0.738 \pm 0.077
214.5556	07.4670	-43.60 \pm 0.05	-28.18 \pm 0.05	-102.93 \pm 3.36	-430.78 \pm 11.45	81.29 \pm 1.16	11.2 \pm 0.8	5.1 \pm 0.2	0.37 \pm 0.01	3.5 \pm 0.2	-0.70 \pm 0.04	340.16 \pm 6.67	0.864 \pm -0.042
217.3861	15.1650	6.02 \pm 0.06	-12.35 \pm 0.06	-5.72 \pm 2.14	-41.35 \pm 1.0	-171.37 \pm 1.03	10.9 \pm 0.1	7.5 \pm 0.1	0.19 \pm 0.00	6.4 \pm 0.1	0.71 \pm 0.01	1150.58 \pm 17.37	0.793 \pm -0.002
217.5786	14.0379	-1.42 \pm 0.05	-7.46 \pm 0.04	191.61 \pm 2.64	-361.55 \pm 4.47	-86.38 \pm 1.13	22.5 \pm 1.0	7.5 \pm 0.2	0.50 \pm 0.01	22.4			

Table A1 – continued

RA (deg)	DEC (deg)	pmra ($\mu\text{as yr}^{-1}$)	pmdec ($\mu\text{as yr}^{-1}$)	U (km s^{-1})	V (km s^{-1})	W (km s^{-1})	R_{apo} (kpc)	R_{peri} (kpc)	Eccentricity	Z_{max} (kpc)	J_{ϕ}/d_{\odot}	$J_z/J_{z\odot}$	E/E_{\odot}
218.4622	10.3683	-2.14 \pm 0.07	-8.22 \pm 0.07	-20.40 \pm 0.78	-95.99 \pm 1.48	-130.24 \pm 0.58	7.4 \pm 0.0	4.9 \pm 0.1	0.20 \pm 0.01	4.6 \pm 0.1	0.46 \pm 0.01	968.5 \pm 12.36	1.038 \pm -0.003
228.4607	08.3553	-3.84 \pm 0.07	-59.49 \pm 0.09	192.77 \pm 7.38	-267.75 \pm 10.58	-100.5 \pm 4.25	12.9 \pm 0.7	0.9 \pm 0.1	0.87 \pm 0.01	4.3 \pm 0.2	-0.11 \pm 0.04	261.09 \pm 20.8	0.909 \pm -0.036
228.6557	09.0914	-15.11 \pm 0.05	-33.13 \pm 0.06	-18.70 \pm 3.11	-232.36 \pm 9.37	-135.68 \pm 0.98	7.5 \pm 0.0	0.6 \pm 0.2	0.86 \pm 0.05	7.2 \pm 0.3	-0.0 \pm 0.04	1206.47 \pm 29.75	1.181 \pm -0.002
228.8159	00.2222	-6.67 \pm 0.09	-59.12 \pm 0.11	120.03 \pm 4.60	-223.37 \pm 8.85	-102.83 \pm 4.26	9.7 \pm 0.4	0.4 \pm 0.2	0.92 \pm 0.04	4.1 \pm 0.3	0.03 \pm 0.03	349.16 \pm 37.54	1.104 \pm -0.014
229.1219	00.9089	-31.52 \pm 0.06	-33.97 \pm 0.05	-151.99 \pm 0.39	-409.54 \pm 24.74	-147.89 \pm 0.89	12.9 \pm 1.6	5.2 \pm 0.4	0.43 \pm 0.02	7.8 \pm 0.5	-0.59 \pm 0.08	1122.98 \pm 59.34	0.79 \pm -0.064
233.5730	06.4702	-3.73 \pm 0.04	-6.44 \pm 0.05	47.28 \pm 2.63	-404.88 \pm 9.71	-71.97 \pm 0.93	11.6 \pm 0.8	5.1 \pm 0.5	0.40 \pm 0.02	11.6 \pm 0.8	0.03 \pm 0.02	4111.92 \pm 239.13	0.83 \pm -0.044
235.1449	08.7463	16.68 \pm 0.05	-25.74 \pm 0.05	116.75 \pm 5.29	-104.67 \pm 1.79	-296.21 \pm 4.42	25.6 \pm 1.3	5.2 \pm 0.1	0.66 \pm 0.02	22.0 \pm 1.3	0.45 \pm 0.01	2973.52 \pm 51.91	0.45 \pm -0.026
235.7578	09.0000	-29.80 \pm 0.06	6.08 \pm 0.06	-185.50 \pm 5.42	-144.08 \pm 4.88	133.52 \pm 6.46	12.6 \pm 0.5	1.7 \pm 0.1	0.76 \pm 0.02	6.8 \pm 0.7	0.26 \pm 0.02	663.13 \pm 65.3	0.89 \pm -0.022
236.1068	10.5311	-3.87 \pm 0.04	-4.77 \pm 0.04	49.11 \pm 2.00	-383.69 \pm 8.65	18.86 \pm 1.48	10.2 \pm 0.3	7.3 \pm 0.9	0.17 \pm 0.04	10.1 \pm 0.3	0.14 \pm 0.02	4149.48 \pm 228.01	0.813 \pm -0.038
237.8246	10.1426	-15.19 \pm 0.05	-12.74 \pm 0.04	-70.00 \pm 2.78	-583.25 \pm 36.27	34.02 \pm 10.0	34.6 \pm 18.1	5.8 \pm 0.1	0.67 \pm 0.12	24.7 \pm 15.2	-0.73 \pm 0.03	1998.84 \pm 520.0	0.348 \pm -0.226
237.9600	15.4022	-11.75 \pm 0.04	-23.56 \pm 0.03	-91.49 \pm 2.99	-242.87 \pm 6.53	-188.22 \pm 0.46	8.3 \pm 0.1	4.0 \pm 0.1	0.36 \pm 0.01	8.3 \pm 0.2	-0.06 \pm 0.02	2986.96 \pm 133.31	1.012 \pm -0.006
240.4216	09.6761	1.71 \pm 0.03	-11.53 \pm 0.02	329.53 \pm 14.23	-270.18 \pm 13.16	-177.61 \pm 9.54	47.9 \pm 13.2	3.6 \pm 0.4	0.85 \pm 0.02	41.5 \pm 11.1	0.34 \pm 0.03	2968.97 \pm 414.55	0.157 \pm -0.131
245.4387	08.9954	-25.09 \pm 0.04	-23.90 \pm 0.03	-2.07 \pm 1.29	-316.79 \pm 6.09	29.47 \pm 1.70	6.8 \pm 0.1	1.7 \pm 0.1	0.61 \pm 0.03	1.5 \pm 0.1	-0.28 \pm 0.02	143.66 \pm 8.72	1.292 \pm -0.007
245.5747	06.8844	-0.49 \pm 0.04	11.07 \pm 0.03	-307.45 \pm 11.56	137.48 \pm 13.46	5.32 \pm 8.20	131.2 \pm 56.6	3.2 \pm 0.3	0.95 \pm 0.02	88.0 \pm 33.4	0.51 \pm 0.05	1883.49 \pm 411.94	-0.285 \pm -0.146
245.8356	13.8777	0.98 \pm 0.03	-2.39 \pm 0.02	-76.79 \pm 2.01	-89.61 \pm 1.09	-144.63 \pm 1.55	6.9 \pm 0.1	4.9 \pm 0.1	0.17 \pm 0.02	6.0 \pm 0.1	0.27 \pm 0.01	1865.8 \pm 97.43	1.055 \pm -0.002
246.5144	05.9826	2.42 \pm 0.03	1.45 \pm 0.02	-5.81 \pm 0.40	28.86 \pm 0.75	-17.21 \pm 0.46	10.1 \pm 0.1	6.2 \pm 0.0	0.24 \pm 0.01	2.2 \pm 0.1	0.79 \pm 0.0	189.37 \pm 9.41	0.873 \pm -0.002
246.8588	12.3193	-8.20 \pm 0.03	-5.43 \pm 0.02	-23.27 \pm 1.77	-326.57 \pm 13.64	83.74 \pm 6.31	6.7 \pm 0.7	2.7 \pm 0.6	0.43 \pm 0.11	5.9 \pm 0.6	-0.16 \pm 0.01	1489.34 \pm 239.52	1.226 \pm -0.042
248.4394	07.9229	-7.82 \pm 0.05	-20.68 \pm 0.04	34.18 \pm 1.02	-94.12 \pm 1.82	-18.85 \pm 0.35	7.5 \pm 0.1	3.3 \pm 0.1	0.39 \pm 0.01	0.6 \pm 0.1	0.51 \pm 0.01	29.83 \pm 1.04	1.155 \pm -0.004
248.4959	15.0776	-2.87 \pm 0.03	-11.51 \pm 0.03	277.89 \pm 11.70	-464.93 \pm 15.46	-112.07 \pm 2.48	56.2 \pm 16.2	4.4 \pm 0.5	0.85 \pm 0.02	47.1 \pm 12.6	0.43 \pm 0.06	3269.42 \pm 292.39	0.077 \pm -0.134
250.6963	08.3743	-6.84 \pm 0.04	-1.89 \pm 0.04	-21.03 \pm 0.87	-205.95 \pm 7.35	162.04 \pm 5.92	7.5 \pm 0.3	0.9 \pm 0.2	0.80 \pm 0.03	7.4 \pm 0.4	0.01 \pm 0.01	1634.18 \pm 172.91	1.176 \pm -0.026
251.4082	12.3657	-7.86 \pm 0.06	-1.27 \pm 0.05	-70.42 \pm 2.20	-400.15 \pm 11.31	386.54 \pm 11.06	201.6 \pm 102.4	9.5 \pm 0.7	0.90 \pm 0.03	155.3 \pm 63.8	0.05 \pm 0.03	11689.1 \pm 785.88	-0.444 \pm -0.127
252.1639	15.0648	1.49 \pm 0.03	-5.48 \pm 0.03	94.04 \pm 5.86	-203.86 \pm 3.85	-231.61 \pm 4.19	15.2 \pm 1.1	4.5 \pm 0.2	0.54 \pm 0.01	14.1 \pm 1.0	0.26 \pm 0.02	2869.78 \pm 110.49	0.721 \pm -0.04
253.8582	15.7240	-2.22 \pm 0.03	-5.72 \pm 0.03	88.00 \pm 6.04	-263.85 \pm 8.44	-57.11 \pm 0.63	7.9 \pm 0.6	1.9 \pm 0.2	0.62 \pm 0.04	5.7 \pm 0.5	0.19 \pm 0.02	968.04 \pm 56.69	1.165 \pm -0.031
254.5207	15.4969	14.12 \pm 0.02	-9.85 \pm 0.03	44.56 \pm 0.56	18.18 \pm 0.26	-28.06 \pm 0.72	11.7 \pm 0.1	7.2 \pm 0.1	0.24 \pm 0.00	0.7 \pm 0.1	0.95 \pm 0.0	20.13 \pm 0.98	0.785 \pm -0.001
254.5469	10.9129	-21.80 \pm 0.04	-28.68 \pm 0.04	260.45 \pm 10.30	-383.71 \pm 23.23	133.82 \pm 4.69	25.0 \pm 5.2	2.5 \pm 0.3	0.82 \pm 0.01	20.4 \pm 4.0	-0.28 \pm 0.05	1683.88 \pm 96.41	0.501 \pm -0.11
255.2671	14.9711	-8.81 \pm 0.04	-40.50 \pm 0.04	208.89 \pm 3.70	-210.05 \pm 4.37	-32.63 \pm 0.96	12.1 \pm 0.2	0.7 \pm 0.1	0.88 \pm 0.02	1.0 \pm 0.1	0.16 \pm 0.01	51.85 \pm 1.75	0.96 \pm -0.01
255.5555	10.8612	-5.06 \pm 0.04	-15.51 \pm 0.04	-108.68 \pm 9.34	-418.27 \pm 13.88	-213.57 \pm 1.85	12.8 \pm 1.0	5.5 \pm 0.2	0.40 \pm 0.04	8.9 \pm 0.4	-0.55 \pm 0.02	1544.81 \pm 66.8	0.781 \pm -0.028

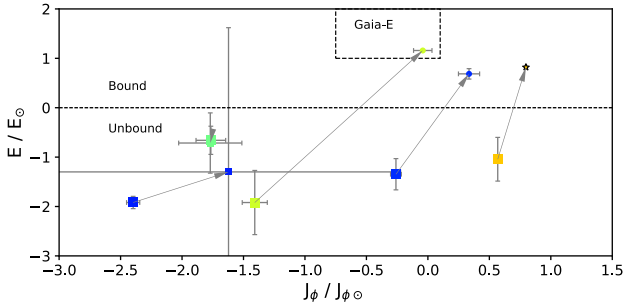


Figure A1. Comparison of the orbital parameters for five stars with unbound orbits from the dynamical analysis in Section 6.1. Large symbols are the parameters using the distances from the Bayesian inference method, and small symbols are those from adopting $1/\text{parallax}$ from the *Gaia* DR2 data base. Points coloured by $[\text{Fe}/\text{H}]_{\text{Q6}}$ using the same scheme same as in Fig. 16.

higher ($\log g = 2.3$, may be closer to $\log g \sim 3$). In that case, we find small corrections to the abundances, such that $\Delta \log(\text{Fe II}) \sim +0.3$, bringing Fe II into much better agreement with Fe I. The impact on $[\text{Fe}/\text{H}]$ for this star is negligible though since the iron abundance is dominated by the more numerous spectral lines of Fe I. Minor adjustments to the other elements would have no significant effect on the chemical analysis and interpretation of this star.

Finally, when examining the impact of the distances for the two stars Pristine_182.5364 ($[\text{Fe}/\text{H}] = -1.6$) and Pristine_181.4395 ($[\text{Fe}/\text{H}] = -2.8$), we find that they always result in highly retrograde and unbound orbits. The orbit for the more metal poor of these two stars is highly uncertain when determined from its parallax ($\Delta\pi/\pi = 0.45$). Interestingly though, this star is also one of the $[\text{Ba}/\text{Fe}]$ -poor stars discussed in Section 5.4 as possibly accreted from an ultra-faint dwarf galaxy. As a sanity check, we also calculated the orbits for all of the other metal-poor candidates in

this analysis, but found only small offsets in their orbit and action parameters.

¹Department of Physics and Astronomy, University of Victoria, Victoria, BC V8W 3P2, Canada

²Université de Strasbourg, CNRS, Observatoire astronomique de Strasbourg, UMR 7550, F-67000 Strasbourg, France

³Leibniz-Institut für Astrophysik Potsdam (AIP), An der Sternwarte 16, D-14482 Potsdam, Germany

⁴Max-Planck-Institut für Astronomie, Königstuhl 17, D-69117 Heidelberg, Germany

⁵Institute of Astronomy, University of Cambridge, Madingley Road, Cambridge CB3 0HA, UK

⁶GEPI, Observatoire de Paris, Université PSL, CNRS, Place Jules Janssen, F-92195 Meudon, France

⁷Université Côte d’Azur, Observatoire de la Côte d’Azur, CNRS, Laboratoire Lagrange, Bd de l’Observatoire, CS 34229, F-06304 Nice Cedex 4, France

⁸Institute of Physics, Laboratoire d’astrophysique, Ecole Polytechnique Fédérale de Lausanne (EPFL), Observatoire, CH-1290 Versoix, Switzerland

⁹Institute of Astronomy, Russian Academy of Sciences, Pyatnitskaya st 48, 119017 Moscow, Russia

¹⁰Department of Astronomy, University of Texas at Austin, Austin, TX 78712, USA

¹¹National Research Council Herzberg Astronomy and Astrophysics, 4071 West Saanich Road, Victoria, BC, V9E 2E7, Canada

¹²Instituto de Astrofísica de Canarias, Via Láctea E-38205, La Laguna, Tenerife, Spain

¹³Departamento de Astrofísica, Universidad de La Laguna, E-38206, La Laguna, Tenerife, Spain

¹⁴UK Astronomy Technology Centre, Royal Observatory Edinburgh, Blackford Hill, Edinburgh EH9 3HJ, UK

¹⁵Department of Astronomy and Astrophysics, University of Toronto, Toronto, ON M5S 3H4, Canada

¹⁶The Oskar Klein Centre, Department of Physics, Stockholm University, AlbaNova, SE-10691 Stockholm, Sweden

This paper has been typeset from a \LaTeX file prepared by the author.